Department of Geomatics Engineering

GPS/INS Integration Aided with Gyroscope-Free IMU for Pedestrian Applications

(URL: http://geomatics.ucalgary.ca/graduatetheses)

by

Anshu Pahadia

December 2010

SCHULICH
School of Engineering   UNIVERSITY OF CALGARY

UNIVERSITY OF CALGARY

GPS/INS Integration Aided with Gyroscope-Free IMU for Pedestrian Applications

by

Anshu Pahadia

A THESIS

SUBMITTED TO THE FACULTY OF GRADUATE STUDIES

IN PARTIAL FULFILMENT OF THE REQUIREMENTS FOR THE

DEGREE OF MASTER OF SCIENCE

DEPARTMENT OF GEOMATICS ENGINEERING

CALGARY, ALBERTA

DECEMBER, 2010

Abstract

This thesis investigates the use of a distributed configuration of accelerometers known as a gyroscope-free inertial measurement unit (GFIMU) as an aid to GPS/INS integration. While a GFIMU is theoretically capable of replacing a traditional strapdown IMU, there are several practical issues that make the approach less than ideal. Therefore, a combination of a GFIMU and a tri-axial gyroscope, referred to as GFIMU+ herein, is designed and tested. Inertial navigation with a GFIMU+ is called Gyroscope free inertial navigation + (GFIN+).

The primary piece of equipment required for the formation of a GFIMU+ is the associated configuration of accelerometers. Five MEMS IMUs were rigidly attached to a compact, Delrin® block for a prototype GFIMU+. The five tri-axial accelerometer measurements and tri-axial gyroscope measurements are combined in an Extended Kalman Filter (EKF) to obtain an estimate of angular velocity. The specific force and angular velocity estimates are inputs to the GPS/INS tight integration software.

Methods used to de-noise inertial sensor measurements are discussed and implemented. The de-noised measurements are used to estimate the de-noised GFIMU+ estimates.

The performance of the GFIN+ system is evaluated in the field in different operating environments and different placements of the GFIMU. The results show that de-noising improves the results in most of the cases and an average improvement of about 30% horizontal RMS is seen as compared to GPS integrated with single MEMS based INS.

Acknowledgements

First of all, I would like to thank my supervisor Dr. Gérard Lachapelle, for supporting, encouraging and guiding me during my MSc studies. I would also like to especially thank him for believing in me and giving a chance in this field of GNSS positioning and navigation. Sincere thanks to my co-supervisor, Dr. Thomas Williams who was always available for lengthy discussions and guiding me throughout my research. His detailed and thorough proof-reading of the chapters of this thesis helped me in further improving this dissertation. He was also very kind to help me with my data collection for this research.

I would like to especially thank my husband, Saurabh, who introduced me to this field. His constant love, support and encouragement all through the two years helped me finish my MSc. I was very lucky as he was always available for me to answer my countless questions.

I would also like to acknowledge my past and present friends. It was because of their belief I was able to achieve everything I have. I am thankful to Pratibha, Kannan, Shashank, Nikita and Rahul because of whom I was able to enjoy some light moments in the university. I am grateful to Antonio and Haris who helped me a lot during data testing. I would further like to extend my appreciation to members and ex-members of the PLAN group for their help in various ways during my studies.

Most of all I would like to thank my family for their love, encouragement and understanding all through my life. Thank you Ma, Papa, Niki, Bablu, Kota Mummy and Kota Papa. This work would not have been possible without your support and good wishes.

Dedication

To Mommy, Papa

&

Saurabh

Table of Contents

List of Tables

List of Figures

List of Symbols

Symbol		Definition
$\dot{x}$	…	Time Derivative of x
$\tilde{x}$	…	Measured quantity of x
$()^q$	…	Quantity in q frame
$()^*$	…	Complex Conjugate of the quantity
$()_k$	…	Quantity at epoch k
$()_m$	…	Quantity along m direction (m can be x, y, z)
$\|\ \|_2$	…	Spectral Norm of the quantity
$D()$	…	Diagonal Matrix of the corresponding vector
$\mathbf{I}$	…	Identity Matrix
$\mathbf{M}$	…	Configuration Matrix
$\mathbf{N}$	…	Non-orthogonality Matrix / Pseudo-Inverse of $\mathbf{M}$
n	…	Length of the observation
$\mathbf{P}$	…	State Covariance Matrix
$\mathbf{Q}$	…	Process Noise Covariance Matrix
$\mathbf{Q}_X$	…	Covariance Matrix of the noise of sensor X
$\mathbf{R}$	…	Measurement Noise Covariance Matrix
$\mathbf{R}_p^q$	…	Rotation matrix from 'p' frame to 'q' frame
$\mathbf{S}$	…	Scale factor error
$\mathbf{S}()$	…	Skew-Symmetric Matrix of a vector
$\mathbf{a}$	…	Acceleration vector
$\mathbf{b}$	…	Constant bias
$\mathbf{f}$	…	Specific force vector
g	…	Gravity vector
n	…	Number of tri-axial accelerometers
$\mathbf{r}$	…	Position vector
S	…	Scale parameter
t	…	Time/ Threshold for wavelet thresholding
$\mathbf{v}$	…	Velocity vector
$\mathbf{v}_i$	…	Vector pointing in direction of ith accelerometer
$\mathbf{v}_k$	…	Measurement Noise at epoch k
$\mathbf{w}_k$	…	Process Noise at epoch k
Δt	…	Time increment
$\Delta\mathbf{v}^p$	…	Velocity increment expressed in 'p' frame
$\boldsymbol{\alpha}$	…	Angular Acceleration vector of body
θ	…	Vertical rotation angle for the calibration block
θ_{mn}	…	Misalignment angle between accelerometer axes m and n
$\Delta\boldsymbol{\theta}_{qr}^p$	…	Angular increment of frame 'r' with respect to frame 'q',

		expressed in frame 'p'
$\mathbf{\Theta}_{qr}^{p}$	$\cdots$	Skew-symmetric matrix of $\Delta\theta_{qr}^{p}$
φ	$\cdots$	Horizontal rotation angle for the calibration block
ϕ	$\cdots$	Latitude
λ	$\cdots$	Longitude
$\boldsymbol{\omega}$	$\cdots$	Angular velocity
$\boldsymbol{\omega}_{qr}^{p}$	$\cdots$	Angular Velocity of frame 'r' with respect to frame 'q', expressed in frame 'p'
$\mathbf{\Omega}_{qr}^{p}$	$\cdots$	Skew-symmetric matrix of ω_{qr}^{p}
ξ	$\cdots$	Roll
η	$\cdots$	Pitch
$\boldsymbol{\eta}_{X}$	$\cdots$	Random Noise of Sensor X
σ	$\cdots$	Standard Deviation of the Noise of Signal
Ψ	$\cdots$	Continuous Wavelet Transform
ψ	$\cdots$	Azimuth
ψ	$\cdots$	Mother wavelet function
τ	$\cdots$	Translation parameter

List of Abbreviations

Abbreviation		Definition
C/A-code	…	Coarse/Acquisition code
CCIT	…	Calgary Center for Innovative Technology
CDMA	…	Code Division Multiple Access
CWT	…	Continuous Wavelet Transform
DoD	…	Department of Defense
DR	…	Dead Reckoning
DWT	…	Discrete Wavelet Transform
ECEF	…	Earth Centered Earth Fixed
EKF	…	Extended Kalman Filter
ENU	…	East North Up
GFIMU	…	Gyroscope free inertial measurement unit
GFIN	…	Gyroscope free inertial navigation
GM	…	Gauss Markov
GNSS	…	Global Navigation Satellite System
GPS	…	Global Positioning System
HPF	…	High Pass Filter
IDWT	…	Inverse Discrete Wavelet Transform
IMU	…	Inertial Measurement Unit
INS	…	Inertial Navigation System
LC	…	Loose Coupling
LLF	…	Local Level Frame
LOD	…	Level of Decomposition
LPF	…	Low Pass filter
MEMS	…	Micro-electromechanical Systems
P-code	…	Precise code
PDR	…	Pedestrian Dead Reckoning
PLAN	…	Position, Location and Navigation
PPM	…	Parts-per-Million
PPS	…	Pulse per second
PRN	…	Pseudo Random Noise
RMS	…	Root Mean Square
RTS	…	Rauch Tung Streibel
SN	…	Serial Number
TC	…	Tight Coupling
USNO	…	United States Naval Observatory
WMRA	…	Wavelet Multi-Resolution Analysis
ZUPT	…	Zero Velocity Update

Chapter One: Introduction

1.1 Background

In recent years, interest in pedestrian navigation has expanded significantly. The Global Positioning System (GPS) and Inertial Navigation System (INS) are now being used for positioning and attitude determination in a wide range of applications. Pedestrian navigation applications, like locating emergency workers (fire fighters and rescue workers), locating callers to emergency services, sports applications, guiding visitors around a shopping mall or exhibition, etc., are the main driving force for the demand and growth of positioning and navigation products. Moreover, the Enhanced 911 (E911) mandate is a main thrust in the growth and development of pedestrian navigation systems (PNS) as it requires the cellular network operators to locate the users within an accuracy of 300 m within 6 minutes (FCC 2010). This is new change in the mandate which also requires the accuracy rates requirements to be met by September, 2012.

The issue of positioning and navigation might appear fairly easy to resolve given technologies like GPS, which have been fully operational for about 15 years. However, real life situations encountered by pedestrians include those areas where GPS signals are blocked or severely degraded (such as indoor, urban and forest areas). In recent years PNS have integrated additional sensors with Global Navigation Satellite Systems (GNSS). One such system is an INS, which has complementary characteristics to GPS

and therefore, an integrated solution can provide continuous, reliable and accurate solution.

Micro-electromechanical systems (MEMS) inertial sensors are an attractive option for a PNS, because of their many advantages, such as small size, low cost, and low power consumption. Although MEMS accelerometers have undergone considerable improvement and can now be found in near tactical grade systems (Kennedy & Rossi 2008), MEMS gyroscopes are still not of sufficient quality to allow stand-alone Strapdown Inertial Navigation (SIN) for extended periods of time. They feature large bias drifts, turn-on to turn-on variability, low shock resistance and poor durability that limit the performance of free inertial navigation. Moreover, gyroscopes are considerably more costly than accelerometers. Therefore, techniques of using multiple MEMS gyroscopes combined by the use of an optimal estimation scheme (Bayard & Ploen 2005), and that of multiple IMUs (Bancroft 2008) to improve the GPS/INS integrated solution are expensive. Therefore, in this work, a group of accelerometers are used to determine both the specific force and angular estimates of the body. This group of accelerometers attached to a rigid body is called a gyroscope-free IMU (GFIMU). As will be discussed, there are some problems in using a GFIMU, which can be addressed by combining it with a tri-axial gyroscope. Therefore, the combination of a single tri-axial gyroscope with an accelerometer configuration is studied, which is called GFIMU+. In addition to this, as measurements from the MEMS sensors are generally very noisy, de-noising techniques applied to inertial sensor signals are discussed and implemented. The de-noised measurements are then used to determine the de-noised angular velocity measurements. It

is shown that de-noising the measurements improves performance and an average improvement of about 30% horizontal RMS is seen as compared to GPS integrated with single MEMS based INS (termed as SIN).

1.2 Overview and Limitations of Previous Research

In recent years, several researchers have investigated the integration of a low cost IMU with GPS, for developing a PNS, for example Kappi et al (2001), Lachapelle et al (2006), Groves et al (2007), and Weimann et al (2007). Most of these contributions dealt with single IMU integrated with GPS. A limitation of this approach is the position drift of the user during GPS blockage or outage. While there are post processing smoothing techniques which can reduce this error (e.g. Rauch-Tung-Streibel (RTS) Smoothing) (Godha 2006), the real time solution is still limited by the drift in position during GPS outages (Bancroft et al 2008).

The increase in quality and decrease in cost of MEMS accelerometers are the main motivation factors driving research on the use of a distributed accelerometer configuration to determine the complete kinematics of the body to which they are attached. The work in which an accelerometer configuration is used includes Cardou & Angeles (2008a), Chen et al (1994), Krishnan (1965), Mital & King (1979), Park et al (2005), Parsa et al (2004), Schuler et al (1967) etc. In all these contributions, the accelerometer configuration used varies according to the number of accelerometers and the shape of the configuration.

There are many applications of using an accelerometer configuration, for example, Mital & King (1975) used it to determine the measurement of the motion of crash-test dummies in impact tests. Mostov et al (1998) investigated the suitability of the cube configuration for automotive applications. Costello (2002) utilized accelerometer measurements to effectively estimate the angular rates and accelerations in a rocket. Ang et al (2003) used a six sensor Gyroscope-free IMU for a medical application. They used three dual-axes accelerometers to sense tremor in hand-held microsurgical instruments.

The minimum number of single-axis accelerometers to determine the complete body dynamics is six (Chen et al 1994). However, by using six accelerometers only the linear and angular accelerations can be estimated. The angular velocity has to be estimated by integrating the angular acceleration. Due to the inbuilt errors in the accelerometer measurements, integration leads to an increase in error with time in the estimation of angular velocity. Furthermore, in certain cases the applied differential equations need angular velocity in order to estimate the angular acceleration (Schuler et al 1967).

Moreover, it is postulated that to obtain reliable angular acceleration results, the required accuracy of the measured data should be approximately one percent of the peak linear acceleration (Padgaonkar et al 1975). This degree of accuracy is usually not attainable with existing MEMS accelerometers.

Therefore, to deal with this issue, many researchers like Cardou & Angeles (2008a), Padgaonkar et al (1975) etc. have used more than six single-axis accelerometers. The former uses four triplets of mutually orthogonal accelerometers, attached to four of the vertices of the parallelepiped, whereas the latter uses a configuration of nine

accelerometers. The redundant sensors are useful as the angular acceleration estimation then does not depend on angular velocity, as those terms can be eliminated from the differential equations. Moreover, with the redundancy, quadratic values for angular velocity can be determined which can be useful for angular velocity estimation.

Zappa et al (2001) concluded that a minimum of 12 single-axis accelerometers are needed to calculate angular velocity for a 6 degree of freedom motion of a body. However, it is not possible to determine the direction of angular velocity as angular velocity is present in its quadratic form (Schopp et al 2010).

Researchers have considered various ways of using the quadratic form in combination with the angular acceleration estimate in order to have a better estimate of angular velocity. Parsa et al (2004) proposed integrating angular acceleration to estimate the sign of the angular velocity. Cardou & Angeles (2008b) proposed to use an Extended Kalman Filter (EKF) with angular acceleration and quadratic angular velocity as measurements. They modeled the angular jerk (time derivative of angular acceleration) as a white sequence and the accelerometer biases as random walks. Park et al (2005) also considered the use of EKF for angular velocity estimation, but did not include bias and angular acceleration states in the filter. Therefore, they did not need to provide a stochastic model for angular acceleration. But since for low cost MEMS sensors, the biases change from turn-on to turn-on, it is very important to determine the biases in the EKF.

Moreover, most of the researchers have used the accelerometer configuration as a standalone system and have not integrated it with a complementary system like GPS, with the exception of few contributions like that of Filho et al (2006), who integrated the

accelerometer derived system with GPS using a loose coupled integration strategy (Section 2.3) and Park & Tan (2002), who used computer simulations to verify the performance of the integrated system. Filho et al (2006) showed that the accuracy of the integrated navigation solution is limited by one standard deviation from GPS measurements, whereas Park & Tan (2002) showed the accuracy to be within 2 sigma bounds and also concluded that GFINS alone looses its accuracy rapidly as compared to GPS/GFINS integrated system.

As measurements from MEMS sensors are generally very noisy, de-noising techniques have been used to de-noise the inertial sensor signals by researchers like Bruton et al (2000), Guo et al (2004), Hamid (2005), and Nassar (2003). Most of the researchers have either used wavelet de-noising techniques or low pass filtering to de-noise the inertial signals, which are then integrated with GPS. This has proven to be successful. However, the de-noising techniques have not been used to test the performance of de-noised angular estimates from accelerometer configuration derived by de-noising accelerometer measurements.

Also, most of the previous research on using a GFIMU has been verified on the basis of computer simulations, however real environment situations are quite different and more difficult because of the presence of random measurement noise, multipath signals and miscellaneous random errors. Therefore, it is important to do a real environment testing analysis, to verify the robustness and reliability of the algorithm.

1.3 Objectives

Given the lack of research in the integrated system of GFIMU+ based inertial navigation and GPS, the main objective of this thesis is to develop and evaluate the ability of multiple accelerometers fixed to a rigid structure to simulate the performance of a single IMU using the theory behind Gyroscope-free IMUs and integrate it with GPS. It also aims to combine the GFIMU with a gyroscope and evaluate the performance of the integrated system in different operating environments and different placements of GFIMU.

With regards to the shortcomings mentioned in the previous section, the objectives and contributions of this work are as follows:

1) Determination of the initial estimates of the errors in the inertial system: Calibration of the inertial sensors is very important, as MEMS sensors generally feature large errors. Moreover, for the correct working of a GFIMU, it is very important to reduce or eliminate the errors associated with the accelerometer measurements. For this purpose, a custom designed calibration rig is used. Specifically a designed calibration procedure also determines the misalignment errors in the sensor architecture.

2) Formation and development of a Gyroscope-free Inertial Navigation + (GFIN+) EKF: A custom designed block of five IMUs is used to form a GFIMU. In this work, similar to Park et al (2005), angular acceleration is not included as state in the EKF but is used to propagate the estimate of angular velocity. However, the

biases are included in states in EKF. This is important because of the turn-on to turn-on variability in biases of MEMS sensors.

3) De-noising the measurements: The operations on the accelerometer measurements increase errors and noise in the angular estimates derived from the GFIMU+. Therefore in this work, the accelerometer measurements are de-noised using both de-noising techniques: wavelet de-noising and low pass filtering. The results are compared on the basis of horizontal RMS position errors with respect to the original measurements.

4) Real environment tests and overall system performance: Tests are done in a variety of operational conditions by using the GFIMU on different parts of the body and the positioning accuracy is assessed of the integrated system both before and after the de-noising. Simulated GPS outages are also used to assess the performance in GPS line-of-sight environments.

1.4 Outline

This five remaining chapters of this thesis are organized in the following manner.

Chapter 2 provides an overview of the fundamentals of GPS and INS. It briefly discusses GPS and describes the errors associated with it. Following this discussion, INS is introduced, along with a discussion of the co-ordinate frames, mechanization equations and the errors sources. The chapter concludes by discussing GPS/INS integration methods.

Chapter 3 describes the benefits and disadvantages of a GFIMU. It introduces the accelerometer configuration used in this work, and describes the method used for its calibration. It also discusses the concept of GFIMU in more details, including the mathematical formulation. Subsequently, the concept of GFIMU+ and GFIN+ is explained. This chapter also provides the design of the GFIN+ Kalman filter.

Chapter 4 discusses the techniques used to de-noise the inertial sensor signals. This chapter begins with discussion on the frequency spectrum of the inertial sensor measurements. Wavelet de-noising technique is presented first, which includes a discussion on wavelet transform. This is followed by low pass filtering de-noising. The chapter concludes with the comparison between the two methods of de-noising.

Chapter 5 provides descriptions of the field tests and the analysis procedure. It presents the performance testing results of GPS/GFIN+ and GPS/De-noised GFIN+ integrated systems in both open and urban areas. The accuracy is tested by simulating outages in the GPS line of sight environments. In the urban test, the accuracy is tested on the basis of horizontal RMS errors present in the solution.

Chapter 6 summarizes the work presented in this dissertation, and draws conclusions from the test results and analysis. Finally, it makes some recommendations for future work.

Chapter Two: Overview of Navigation Systems

This chapter gives a brief review of the fundamentals of GPS and Inertial Navigation Systems. Section 2.1 briefly discusses GPS. In Section 2.2, INS is discussed explaining the different reference coordinate frames, INS mechanization and the error sources. The chapter concludes by briefly describing GPS/INS integration methods.

2.1 Global Positioning System

GPS is a satellite based navigation system developed by the United States Department of Defense (US DoD). GPS provides accurate three dimensional positions, velocities and time information to a user anywhere in the world at any time during any weather condition. This all-weather, worldwide, radionavigation system allows the user to determine range from a satellite by measuring the transit time of the signal and thus, evaluating the user's position using trilateration.

GPS is a passive ranging system with spread spectrum Code Division Multiple Access (CDMA) signals. Each GPS signal consists of three components (Misra & Enge 2004):

- Carrier: The GPS signals are transmitted at two frequencies L1 (1575.42 MHz) and L2 (1227.60 MHz) from all the satellites. A third frequency L5 (1176.45 MHz) is being implemented on upcoming block IIF satellites.

- Ranging code: Modulated on these carriers are Pseudo Random Noise (PRN) codes, which are Coarse/Acquisition (C/A) code on L1 and Precision (encrypted) [P(Y)] code on both L1 and L2. The P-code's access is limited to authorized users

via its encryption by a Y-code. Each satellite has a different sequence of PRN code. This differentiates the transmit information from one satellite to another. Currently there are eight satellites broadcasting an L2C code on L2. (USNO 2010).

- Navigation data: This is a binary coded message modulated on the carrier and consists of data on the satellite health status, and its position and time.

For this work, single frequency L1 measurements were used to integrate with INS, as discussed in Section 2.2. The following three types of measurements can be obtained from a single frequency GPS receiver:

- Code-phase measurements (Pseudoranges): The pseudorange measurements are obtained from the receiver by matching the C/A code received from a GPS satellite with a receiver's internally generated code. Thus it is measured as the amount of time shift required to align the received and generated code and is defined as the transit time multiplied by the speed of light. These measurements are referred to as pseudoranges rather than ranges because the clocks of the satellites and the receiver are not perfectly synchronized to GPS time (Godha 2006).

- Carrier-phase measurements: The carrier phase measurement is much more precise than the code phase measurement and is measured as the difference between the phases of the receiver-generated carrier signal and the carrier received from a satellite at the instant of the measurement. It is generally used for

high-accuracy (cm-level) applications like geodetic surveying and automatic vehicle applications (ibid).

- Doppler measurements: The derivative of the carrier phase measurement with respect to time is called the Doppler frequency. The Doppler measurement is determined by the frequency change of the carrier signal, due to the relative motion of the receiver and the satellite. These measurements, when scaled by the L1 wavelength provide the range rate measurement which can be measured in m/s. This provides the relative velocity between the receiver and the satellite and thus can be used to estimate the velocity of the receiver.

The ability to obtain accurate position, velocity and time from satellite navigation signals depends upon the predictability and controllability of the measurement errors. Thus, it is important to know the major sources of errors and the ways to mitigate them, to obtain the user position solutions with desired performance levels. Errors in GPS signals can be grouped into three categories: Satellite based errors, propagation errors and receiver based errors (Lachapelle 2008). Satellite based errors consist of satellite clock and orbital errors. The propagation errors mainly consist of ionospheric, tropospheric and multipath errors. The receiver based errors are due to the receiver clock and receiver thermal noise. The detail of these errors and their mitigation techniques is not discussed here and can be found in a number of references including Godha (2006), Hide (2003), Misra & Enge (2004) and Petovello (2003).

2.2 Inertial Navigation System

INS is a dead reckoning (DR) system which provides position, velocity and heading information. A DR system is that in which a current state is evaluated by the relative increment from the previous known state. INS is based on measurements obtained from an Inertial Measurement Unit (IMU). A typical IMU consists of three accelerometers and three gyroscopes mounted in orthogonal triads. The measurements from these accelerometers and gyroscopes are combined using mechanization equations (Section 2.2.2) to form an INS.

The principle of inertial navigation comes from Newton's 2nd law of motion which states that 'Acceleration is proportional to the resultant force and is in the same direction as this force' (El-Sheimy 2009). This external force produces an acceleration which is observed by the accelerometers. This acceleration, when integrated, gives the velocity which if integrated again gives the change in position relative to the initial point. Through appropriate initialization, INS is capable of continuous determination of absolute values of position, velocity and attitude.

However in an actual system, these integrations are accomplished after appropriate processing of the data which involves rotating the data in the desired frame. This drives the need for gyroscopes in the system. Integration of angular measurements from gyroscopes provides change in attitude of the system, which when combined by initial attitude provides the new attitude of the system. Attitude is defined by rotations along the three axes which are called roll, pitch and azimuth or yaw. In this work, roll is defined as rotation along the y axis, pitch is rotation along the x axis and azimuth is rotation along

the z axis. Based on the attitude parameters the rotational relation is established between the IMU *body frame* and the *navigation frame* (Section 2.2.1), which is used for rotating the accelerations (El-Sheimy 2009, Godha 2006 and Petovello 2003).

Errors in gyroscope measurements will therefore lead to errors in acceleration and finally position. For example, a gyroscope bias (Section 2.2.3.2) introduces a quadratic error in velocity and a cubic error in position (El-Sheimy 2009). Therefore, the quality of an IMU and thus an INS is often judged by the quality of gyros contained in the sensor system (ibid).

2.2.1 Coordinate Frames

There are four coordinate frames which are generally used when considering inertial navigation systems. These definitions follow from El-Sheimy (2009), Godha (2006), Petovello (2003) and Shin (2001). The superscript denotes the frame in which a measurement is obtained.

Inertial Frame (*i*-frame) is considered to be non-rotating and non-accelerating frame relative to far-off galaxies (Petovello 2003). The origin of the inertial frame is arbitrary, and the co-ordinate axis may point in any three mutually perpendicular directions (Farrell & Barth 1999). But for practical purposes, an inertial frame is defined as follows:

Origin: Earth's center of mass

Z^i-axis: Parallel to spin axis of the Earth

X^i-axis: Pointing towards the mean vernal equinox

Y^i-axis: Orthogonal to X and Z completing the right hand system

Earth Centered Earth Fixed frame (ECEF or *e*-frame) is defined as follows:

Origin: Earth's center of mass

Z^e-axis: Parallel to mean spin axis of the Earth

X^e-axis: Pointing towards the mean meridian of Greenwich

Y^e-axis: Orthogonal to X and Z completing the right hand system

Local Level Frame (LLF or *l*-frame) is defined as follows:

Origin: Coinciding with the center of the navigation system

Z^l-axis: Orthogonal to reference ellipsoid pointing Up

X^l-axis: Pointing towards geodetic East

Y^l-axis: Pointing towards geodetic North

This forms a right hand East-North-Up (ENU) frame which is shown in Figure 2.1. It also

shows the latitude (ϕ) and longitude (λ) angles.
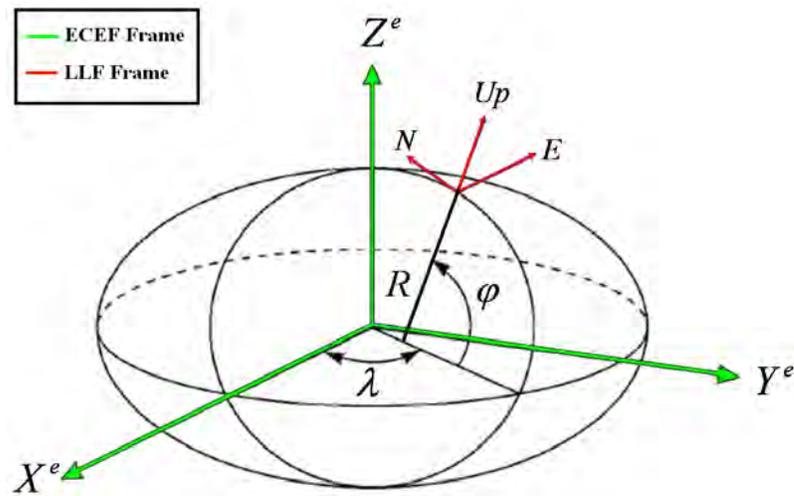
Figure 2.1: ECEF and LLF Frame (Godha 2006)

Body Frame (*b*-frame) is an orthogonal frame that represents the orientation of the body

to which it is connected. The body frame is assumed to be aligned with the pedestrian

frame in such a way so that:

Origin: Center of the IMU or the body comprising multiple IMUs

X^b-axis: Pointing towards the right to the direction of motion

Y^b-axis: Pointing towards the front (in the direction of motion)

Z^b-axis: Pointing up to complete the orthogonal right hand system

The data integration is performed in one of the above frames. This frame is called a

navigation frame. The above mentioned coordinate frames can be transformed from one

frame to another using rotation matrices or quaternions (El-Sheimy 2009).

2.2.2 INS Mechanization Equations

Mechanization equations are the set of equations which are used to convert the specific force (f^b) and angular velocity (ω^b) measurements obtained from an IMU into position, velocity and attitude information (Godha 2006). Users can select any coordinate frame as the navigation frame depending on the application requirements. Such a choice mainly depends on the system designer and/or system requirements. In this work, the ECEF frame is used for mechanization implementation for two main reasons (Godha 2006, Petovello 2003):

1. The mechanization equations are easy to implement and are less computationally intensive than LLF, and

2. The integration of INS with complementary technology (like GPS) becomes easier as GPS provides position/velocity in ECEF frame.

The accelerometer output is specific force measurement (f^b) which is related to body acceleration (a^b), via gravitational acceleration (g), as follows (Petovello 2003):

$$f^b = a^b - g^b.$$
(2.1)

Therefore, the body acceleration is computed using Equation (2.1) before integrations are performed. Also, a gyroscope senses the angular rates due to Earth rotation and the rotation due to body movement. To get the actual body angular velocity, the Earth rotation rate should be transformed into the body frame and removed from the measured angular rates. The mechanization equation in the ECEF frame is given by

$$
\begin{bmatrix} \dot{r}^e \\ \dot{v}^e \\ \dot{R}_b^e \end{bmatrix} = \begin{bmatrix} v^e \\ R_b^e f^b - 2\Omega_{ie}^e v^e + g^e \\ R_b^e (\Omega_{ei}^b + \Omega_{ib}^b) \end{bmatrix}
\tag{2.2}
$$

where the dots denote the time derivative. The angular velocity vector ω_{yz}^x represents the angular velocity of frame 'z' with respect to frame 'y', expressed in frame 'x'. The symbols denote the following quantities:

r^e … is the position vector,

v^e … is the velocity vector,

R_b^e … is the rotation matrix from body frame to ECEF frame,

f^b … is the specific force measured by the accelerometer triad,

Ω_{ie}^e … is the skew-symmetric matrix of the Earth rotation rate ω_{ie}^e,

g^e … is the gravity vector,

Ω_{ei}^b … is the skew-symmetric matrix of the rotation rate ω_{ei}^b, and

Ω_{ib}^b … is the skew-symmetric matrix of the measured angular rate ω_{ib}^b.

As can be seen, the specific force (f^b) and the angular rate measurements (ω_{ib}^b) measured by the IMU act as input to the mechanization equations. Figure 2.2 shows the INS mechanization block diagram.
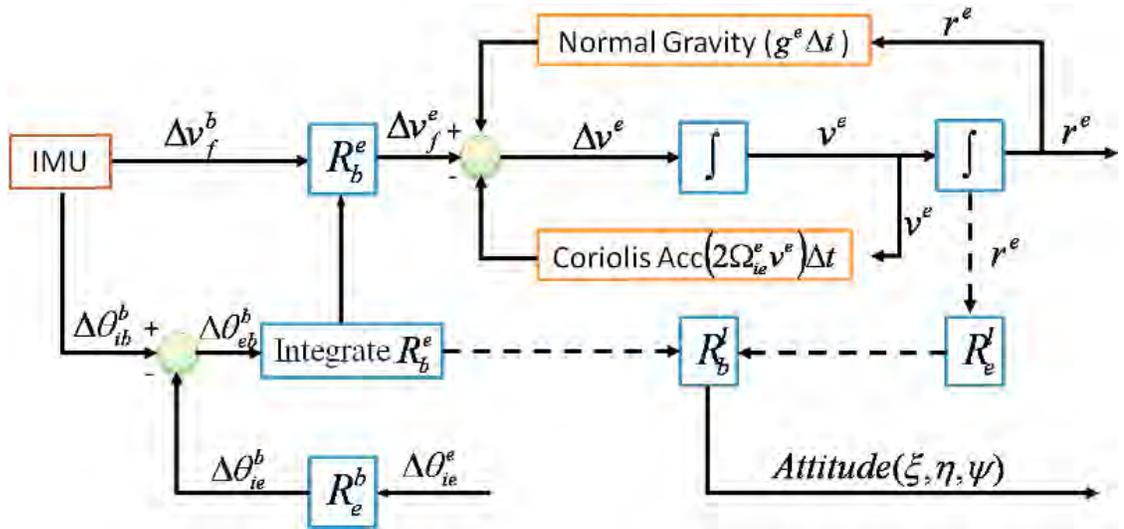
Figure 2.2: INS Mechanization in ECEF Frame (Adapted from El-Sheimy 2009, Godha 2006)

The velocity and angular increments can be obtained from the specific force and angular velocity measurements from the IMU as explained in Section 2.2.2.3. They are input into the INS mechanization system. The angular increment $\Delta\theta_{ib}^{b}$, when combined with the Earth's angular velocity increment $\Delta\theta_{ie}^{b}$, gives the angular increment of body with respect to earth expressed in body frame, $\Delta\theta_{eb}^{b}$. This vector can be used to update the R_{b}^{e} matrix, which can be used to transform the velocity increment in body frame to ECEF frame, Δv^{e}. This is then corrected for Coriolis acceleration and gravity corrections and integrated to give the velocity v^{e} and position r^{e} vectors.

The mechanization Equation (2.2) can be solved by the following basic steps (El-Sheimy 2009, Godha 2006 and Petovello 2003):

- Sensor error correction

- Attitude update

- Transformation of specific force to navigation frame (here e-frame)

- Velocity and Position Calculation.

2.2.2.1 Sensor error correction

The raw measurements obtained from a low cost IMU are generally corrupted by errors such as constant bias, bias drift, scale factor errors and axis non-orthogonalities. These errors will be described in Section 2.2.3. The values for these errors are estimated from lab-calibration and during the navigation process in the Kalman Filter of a GPS/INS integrated system (Petovello 2003). Chapter 3 describes a calibration procedure for a GFIMU.

Once the errors such as bias and scale factor have been estimated, the gyroscopes and accelerometers measurements can be corrected as follows:

$$
\left(\Delta\theta_{ib}^{b}\right)_{p} = \frac{\left(\left(\Delta\tilde{\theta}_{ib}^{b}\right)_{p} - \left(b_{g}\right)_{p}\Delta t\right)}{\left(1 + \left(S_{g}\right)_{p}\right)}
\tag{2.3}
$$

$$
\left(\Delta v_{f}^{b}\right)_{p} = \frac{\left(\left(\Delta\tilde{v}_{f}^{b}\right)_{p} - \left(b_{a}\right)_{p}\Delta t\right)}{\left(1 + \left(S_{a}\right)_{p}\right)}
\tag{2.4}
$$

where , '~'   … represents the raw measurements

$(`.`)_{p}$ … are respective quantities along p (x, y or z) direction

$\Delta\theta_{ib}^{b}$ … is the angular increment of body in body frame

Δv_{f}^{b} … is the velocity increment of body in body frame

b_a, b_g ... are the biases for each sensor,

S_a, S_g ... are the scale-factor errors for each sensor,

Δt ... is the time increment $(t_{k+1} - t_k)$.

2.2.2.2 Attitude update

The body angular rates with respect to ECEF frame are given by (as in last row of Equation (2.2)):

$$\omega_{eb}^b = \omega_{ib}^b - \omega_{ie}^b = \omega_{ib}^b - R_e^b \omega_{ie}^e \tag{2.5}$$

where R_e^b is the rotation matrix from the ECEF to the body frame.

The first term, ω_{ib}^b, is obtained directly from the gyroscope measurements while the second term comprises the Earth rotation rate which is a known constant. Thus, inputting ω_{ib}^b, ω_{ie}^e and the rotation matrix R_e^b, the total angular velocity of the body can be obtained. In terms of angular increments Equation (2.5) is

$$\Delta \theta_{eb}^b = \Delta \theta_{ib}^b - \Delta \theta_{ie}^b \tag{2.6}$$

where $\Delta \theta_{ie}^b = R_e^b \omega_{ie}^e \Delta t$.

The rotation matrix, R_e^b, depends on time and can be updated by using the new angular increment equation:

$$\dot{R}_e^b = R_e^b \Omega_{eb}^b. \tag{2.7}$$

The solution of Equation (2.7) for a constant coefficient matrix Ω_{eb}^b is:

$$R_e^b\left(t_{k+1}\right) = R_e^b\left(t_k\right)\exp\left(\Omega_{eb}^b t\right) \tag{2.8}$$

where $\exp\left(\Omega_{eb}^b t\right)$ is a matrix exponential. The equation of skew symmetric matrix

Θ_{eb}^b using computed angular increments $\Delta\theta_{eb}^b(\Delta\theta_x^b, \Delta\theta_y^b, \Delta\theta_z^b)$ can be written as (El-Sheimy 2009):

$$\Theta_{eb}^b = \begin{bmatrix} 0 & -\Delta\theta_z^b & \Delta\theta_y^b \\ \Delta\theta_z^b & 0 & -\Delta\theta_x^b \\ -\Delta\theta_y^b & \Delta\theta_x^b & 0 \end{bmatrix}. \tag{2.9}$$

Expanding the matrix exponential into an infinite series gives:

$$\exp\left(\Omega_{eb}^b t\right) = \sum_{n=0}^{\infty} \frac{1}{n!}\left(\Theta_{eb}^b\right)^n. \tag{2.10}$$

Substituting Equation (2.10) in Equation (2.8) yields the following recursive relationship

of R_e^b:

$$(R_e^b)_{k+1} = (R_e^b)_k \sum_{n=0}^{\infty} \frac{1}{n!}\left(\Theta_{eb}^b\right)^n \tag{2.11}$$

where $R_e^b\left(t_{k+1}\right)$ has been replaced by $(R_e^b)_{k+1}$.

Expanding Equation (2.11), the following compact solution can be obtained:

$$(R_e^b)_{k+1} = (R_e^b)_k \left(I + \frac{1}{\theta}\sin\theta\ \Theta_{eb}^b + \frac{1-\cos\theta}{\theta^2}\left(\Theta_{eb}^b\right)^2 \right) \tag{2.12}$$

where $\theta = \sqrt{(\Delta\theta_x^b)^2 + (\Delta\theta_y^b)^2 + (\Delta\theta_z^b)^2}$.

Using the updated rotation matrix, a rotation matrix, R_b^l, can be estimated to calculate the

attitude of the body.

$$R_b^l = R_1\left(90° - \phi\right)R_3\left(\lambda + 90°\right)R_b^e \tag{2.13}$$

where ϕ is the latitude of IMU

λ is the longitude of the IMU

R_i is the rotation matrix about the ith axis

Using the rotation matrix R_b^l, the attitude can be estimated using the following formulae:

$$\xi = -\tan^{-1}\left(\frac{(R_b^l)_{3,1}}{(R_b^l)_{3,3}}\right) \tag{2.14}$$

$$\eta = \sin^{-1}\left((R_b^l)_{3,2}\right) \tag{2.15}$$

$$\psi = \tan^{-1}\left(\frac{(R_b^l)_{1,2}}{(R_b^l)_{2,2}}\right) \tag{2.16}$$

where ξ is roll of the body

η is the pitch of the body

ψ is the azimuth/ yaw of the body, and

$(R_b^l)_{p,q}$ is the element of the pth row and the qth column of (R_b^l) matrix.

2.2.2.3 Transformation of specific force to ECEF frame

In this step, the velocity increment (Δv_f^b) or the specific force measurements (f^b) are rotated into the navigation frame (*e*-frame) before integration.

$$f^e = R_b^e f^b \tag{2.17}$$

Integrating f^e, Δv_f^e can be obtained as follows (El-Sheimy 2009):

$$\Delta v_f^e = \int_{t_k}^{t_{k+1}} R_b^e(t) f^b(t) dt .$$ (2.18)

Since the rotation matrix, R_b^e, is a function of time, the average orientation of the IMU during the interval t_k to t_{k+1} is used to calculate Δv_f^e (Godha 2006, Kwakkel 2008, and Petovello 2003). Either Equation (2.19) or (2.20) can be used to estimate velocity increment in ECEF frame, Δv_f^e:

$$\Delta v_f^e = (R_b^e)_k \left(I + \frac{1}{2} \Omega^b \right) \Delta v_f^b$$ (2.19)

$$\Delta v_f^e = (R_b^e)_{k+1} \left(I - \frac{1}{2} \Omega^b \right) \Delta v_f^b$$ (2.20)

where I is an identity matrix, and Ω^b is a skew-symmetric form of the angular increments in Equation (2.6).

2.2.2.4 Velocity and Position Calculation

Using Equation (2.2), the total body velocity increment vector is obtained by

$$\Delta v^e = \Delta v_f^e - 2\Omega_{ie}^e v_k^e \Delta t + g^e \Delta t .$$ (2.21)

The second term in the above equation is called the Coriolis correction, and the third term is called the normal gravity correction. Using the velocity increment, the velocity at epoch t_{k+1} can be estimated. The position increment can then be obtained using:

$$r_{k+1}^e = r_k^e + \frac{\left(v_{k+1}^e + v_k^e\right)}{2}\Delta t \; . \tag{2.22}$$

Thus, to summarize, during the mechanization process described above, the IMU measurements are used to determine the position and velocity updates or increments and the attitude of the body.

2.2.3 Inertial Sensor Errors

As pointed out in Section 2.2.2.1, the first step in solving the INS mechanization equations is to correct for inertial sensor errors. This section describes the various errors present in the sensors and how they can be estimated. The primary errors in gyroscopes and accelerometers include sensor noise, scale factor errors, constant biases, bias drift and non-orthogonality errors. The inertial sensor measurement equations for accelerometer and gyroscope are given by (El-Sheimy 2009):

$$\tilde{f} = f + b_a + S_a f + Nf + \eta_a \tag{2.23}$$

$$\tilde{\omega} = \omega + b_g + S_g \omega + N\omega + \eta_g \tag{2.24}$$

where '~' denotes the measured value from the sensor, subscript 'a' denotes accelerometer specific errors and subscript 'g' denotes gyroscope specific errors.

f is the true specific force,

ω is the true angular rate,

b is the sensor bias vector,

S is a matrix of linear scale-factor error,

N is a matrix representing the non-orthogonality of sensor triads, and

η is the sensor random noise.

The biases can be determined through lab-calibration procedures (Chapter 3) and can be modeled in the Kalman filter during the estimation process. The sensor noise is modelled stochastically in the estimation process.

2.2.3.1 Noise

Noise is an additional signal resulting from the sensor itself or other electronic equipment that interferes with the measured output signals being measured (El-Sheimy 2009, Godha 2006). It is generally non-systematic and thus cannot be removed from the data using deterministic models. It can only be modeled by stochastic means.

The noise parameters that are used for practical purposes can be calculated via two methods: Variance method (Petovello 2003) and Wavelet method (Nassar 2003), details of which can be found in the respective references.

The noise standard deviations calculated using the above methods for the sensors used in this work are summarized in Table 2.1 where SN denotes the serial numbers of the Crista MEMS IMUs used in this work from Cloud Cap Technology Inc.

Table 2.1: Sensor Noise Parameters (Standard Deviation)

	Gyro (º/h)			Accelerometer (m/s^2)		
IMU	*X*	*Y*	*Z*	*X*	*Y*	*Z*
SN 587	595.86	496.19	497.52	0.022	0.032	0.022
SN 868	578.40	613.16	424.29	0.042	0.042	0.047
SN 1245	459.36	459.18	456.40	0.028	0.025	0.024
SN 1246	508.90	445.38	457.77	0.015	0.017	0.015
SN 1039	545.51	516.23	479.23	0.026	0.029	0.025

2.2.3.2 Sensor bias

The sensor bias is defined as an offset in the sensor output which has no correlation with the input acceleration or rotation (Godha 2006, Kwakkel 2008). It is measured in °/h (or rad/s) for gyros and m/s^2 (or mg) for accelerometers.

Bias generally consists of two parts, namely a deterministic part and a stochastic part. The deterministic part is the constant turn-on bias or the bias offset, which refers to the offset in the measurement provided by the inertial sensor. The turn-on bias is the bias in the output when the inertial sensor is turned on and it remains constant for a particular mission. Higher grade sensors like navigation grade IMUs generally have negligible turn on biases. Constant turn on biases can be determined by lab calibration procedures but in lower grade sensors, the turn on variability is high and frequent calibration of these sensors is required. Also, the turn-on biases are estimated in the Kalman filter in an integrated system. The stochastic part is called the bias drift which refers to the rate at which the error in an inertial sensor accumulates with time (El-Sheimy 2009). This is generally modelled as a Gauss Markov (GM) process (Godha 2006).

2.2.3.3 Scale factor errors

A scale factor is the ratio of change in output to change in input intended to be measured (El-Sheimy 2009). Scale factor stability is the capability of the sensor to accurately sense the quantity at different rates. Deviations from the theoretical scale are due to system

imperfections (ibid). Scale factor errors are expressed in parts per million (PPM). These errors can also be modelled stochastically using a suitable random process (El-Sheimy 2009).

2.2.3.4 Non-Orthogonality errors

These errors are the result of misalignment in the axes resulting from the imperfection of mounting the sensors. This causes each axis to measure the measurements of the other two axes in the b-frame. These are denoted by matrix N given by (El-Sheimy 2009):

$$N = \begin{bmatrix} 0 & \theta_{xy} & \theta_{xz} \\ \theta_{yx} & 0 & \theta_{yz} \\ \theta_{zx} & \theta_{zy} & 0 \end{bmatrix} \tag{2.25}$$

where θ_{ab} denotes the misalignment angle between the accelerometer axes, a and b.

2.3 GPS/INS Integration

Since GPS and INS are complementary systems, it is very common to integrate them to provide a continuous and reliable solution. This section describes the various integration strategies to combine GPS and INS. GPS/INS integration can be carried out via following methods (Petovello 2003):

- Loosely coupled
- Tightly coupled
- Ultra-tightly/Deeply coupled

Out of the above, in the ultra-tightly coupled integration strategy, the GPS and INS systems no longer work as independent systems. Instead the GPS updates are used to calibrate INS and the INS is used to aid GPS receiver tracking loops during interference or otherwise degraded signal conditions (Petovello 2003). Since this approach requires access to the receiver's firmware, the end users generally are not able to use this integration strategy. The loosely coupled and tightly coupled integration strategies are quite commonly used and the choice depends on type of application and operating environment. The loosely-coupled integration strategy is the simplest method of coupling, in which INS and GPS receiver generate navigation solutions independently. The information from them is blended using an estimator (Kalman filter) to form a third navigation solution (El-Sheimy 2009). The tightly-coupled integration strategy is also called centralized integration and in this scheme, there is no separate GPS navigation solution filter. A single integration filter is employed to fuse INS and GPS measurements. In this work, the tightly coupled integration strategy (Figure 2.3) is used because of its multiple inherent advantages. First, since in tightly coupled strategy GPS pseudorange and Doppler measurements are used rather than the final calculated positions. There is no requirement of minimum number of satellites and an integrated solution is possible even if there are less than four satellites present, which is generally the case in urban environment and indoor. Second, a single centralized filter provides statistically rigorous sharing of information among states. Also, the process noise is only added to a single filter as compared to loosely coupled strategy where it is added for both the GPS and INS filters (Kwakkel 2008, Petovello 2003).

All these integration strategies can be implemented in one of the following two configurations: Open loop and closed loop configurations. In an open loop configuration, INS errors are estimated using GPS but are not used in the operation of INS, whereas in a closed loop configuration, the sensor errors are compensated within the calculation procedure of the INS mechanization scheme using estimated errors from the Kalman filter (Godha 2006). In the open loop configuration, since the INS errors are not fed back into the INS mechanization loop, the errors grow rapidly. As the INS error model is obtained by linearizing the mechanization equations and neglecting the second order (and higher) terms, this assumption fails when the errors become high, thereby introducing large errors into the integrated system. Therefore, feedback is very important and thus, a closed loop configuration is used. The open loop approach can be useful for high end inertial sensors in which case small errors are propagated.
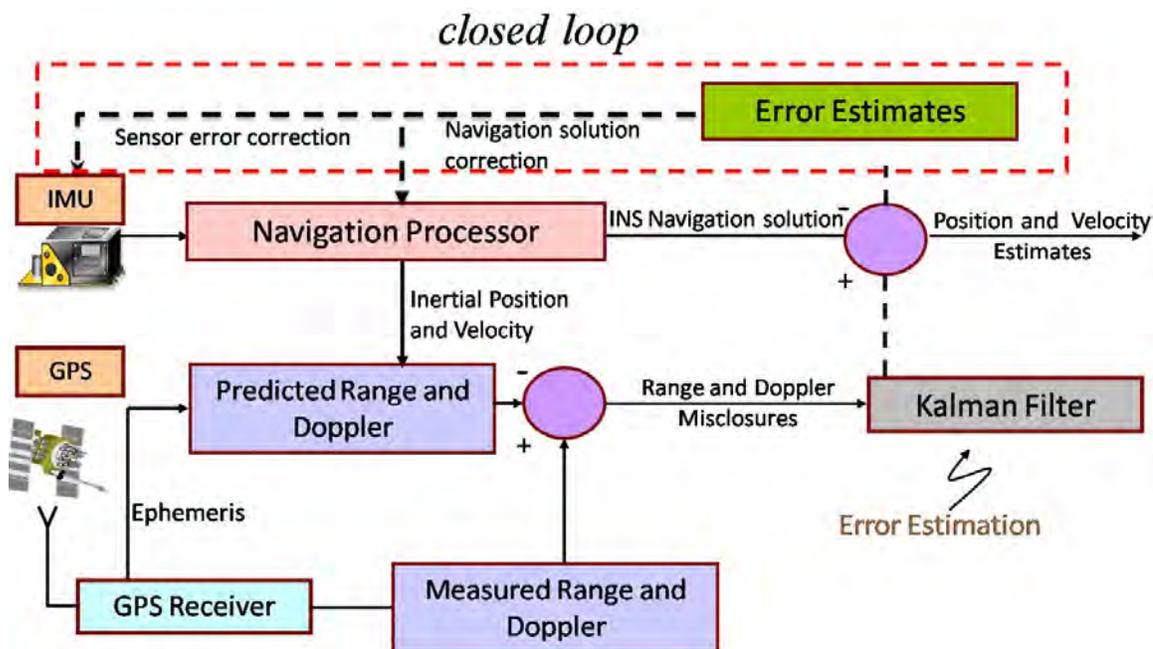

Figure 2.3: Tightly coupled Integration strategy (Adapted from Godha 2006)

Chapter Three: Gyroscope Free Inertial Navigation

Having discussed GPS and INS along with their advantages and disadvantages, this chapter introduces the concept of a gyroscope free IMU and a Gyroscope free Inertial Navigation (GFIN). First, the motivations of using accelerometers instead of gyroscopes to estimate the angular rotation will be discussed. Then, the accelerometer configuration (with 3n accelerometers where n is the number of tri-axial accelerometers) used in this thesis will be introduced. This is followed by some mathematics related to estimation of the kinematics of the instrumented body using the accelerometer measurements. Subsequently the concept of combining a low-cost MEMS gyroscope with the GFIMU, which is here referred to as GFIMU+, is explained. Inertial navigation using GFIMU+ is called GFIN+. Finally, the GFIN+ Kalman Filter design is discussed.

3.1 Background

As explained in Section 2.2, an INS traditionally uses gyroscopes to sense angular motion and accelerometers to sense linear acceleration. However, it is possible to determine the complete kinematics of the body, that is, both the angular velocity and linear acceleration, by using only a set of accelerometers. Since the late 1960s a number of authors have tried to use a configuration of distributed accelerometers to determine the total motion of a rigid body like Krishnan (1965), Schuler et al (1967), Padgaonkar et al (1975) and Mital & King (1979). Such a configuration is here referred to as a Gyroscope-Free IMU. As will be seen in Section 3.2, the basis of a GFIMU design is rigid-body kinematics; the

difference between the acceleration vectors at two points on a rigid body is linearly related to the angular acceleration of the body and quadratically related to the angular velocity. Section 3.1.1 discusses the motivations of using a GFIMU and the problems associated with it.

3.1.1 Benefits and Challenges

There are three major benefits of using a group of accelerometers to determine the angular motion. The first is cost: MEMS accelerometers are considerably lower cost than MEMS gyroscopes; tri-axial MEMS accelerometers are generally in the range of $ 3-6, whereas a comparable single axis gyroscope costs up to $ 50-100 (Digi-key 2010). It should be noted that the number of accelerometers which needs to be ordered to reduce the unit price varies with different manufacturers and different specifications of the accelerometers. But, even when a number of accelerometers are used, they are still generally lower cost than a tri-axial gyroscope. Thus, a GFIMU can be lower cost than a traditional IMU. Secondly, since MEMS accelerometer technology is currently more developed as compared to MEMS gyroscope technology (El-Sheimy 2009), a GFIMU will give potentially better performance than a traditional IMU. The third advantage is that a GFIMU can have substantially larger angular dynamic range than a traditional IMU. A number of applications of a GFIMU were discussed in Section 1.2.

Despite the above stated advantages, there are also many disadvantages to using a GFIMU. Indeed, recently Giansanti et al (2003) concluded, after many simulations, that two previously proposed GFIMUs were not capable of determining position and

orientation of the required accuracy for more than a few seconds in the face of even mild error sources. For example, they concluded that in a time interval of 4 seconds, a minor misalignment error of 0.1 deg can propagate an angular error of approximately 30 deg and a position error of 0.6 m. The source of the disadvantages in a GFIN system can be attributed to the operations that are performed on the accelerometer measurements to get the estimate of the angular velocity. These operations generally involve weighted differences and numerical integration. The numerical integration translates any constant bias errors in the accelerometers' measurements into linearly increasing errors in the angular velocity estimate. Stochastic errors in accelerometer measurements lead to increasing error variances with respect to time. The weighted differencing leads to an increase in noise in the angular estimates of the GFIMU. In lower dynamics case, when the true angular velocity is very small, the noise masks the original motion of the body. Another disadvantage of a GFIMU is initialization because it is not possible to unambiguously estimate the initial angular velocity from accelerometer measurements. These disadvantages are addressed in this work by further integrating a GFIMU with a single tri-axial gyroscope which is the proposed approach of this research discussed in Section 3.5.

3.2 Formation of a GFIMU

As stated earlier, using a configuration of accelerometers to estimate the angular motion has been used by many researchers. Schuler et al (1967) described many configurations with 6, 8 and 9 accelerometers along with pointing out the advantages and disadvantages

of them. The mentioned disadvantages included the ambiguity in the sign of the angular velocity output along with stability issues in integrating a differential equation to determine the angular velocity for a configuration. Chen et al (1993) described the cube shaped configuration with six accelerometers as shown in Figure 3.1, with the arrows representing the accelerometers and pointing in the respective sensing directions.
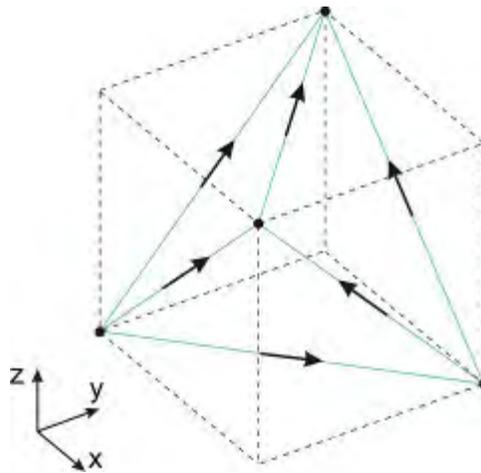
Figure 3.1: Cube-shaped configuration (Bestmann & Hecker 2009, Chen et al 1993)

In this thesis, five tri-axial MEMS accelerometers that are attached to a rigid body are being used, as shown in Figure 3.2. This is a prototype GFIMU which consists of five Crista IMUs from Cloud Cap Technology to a specially designed Delrin® block. The block is custom designed and is approximately 8.5 cm in width and 6.5 cm in height. It has a bolting flange to ensure repeatable and rigid fixation.

**Figure 3.2: Proposed GFIMU composed of five MEMS IMUs attached to a Delrin®
block**

Four of the IMUs are coplanar and are mounted around the periphery of the block on two
pairs of parallel faces and one is on the upper face. Theoretically, at least four non-
coplanar tri-axial accelerometers are required for a feasible accelerometer configuration
capable of determining the angular estimates (Parsa et al 2004). Thus, the above
mentioned configuration is feasible; using its data redundancy benefits can be explored,
as it has an extra tri-axial accelerometer. The choice of using this configuration was
mainly driven by the compactness, repeatability and ease of using the block for data
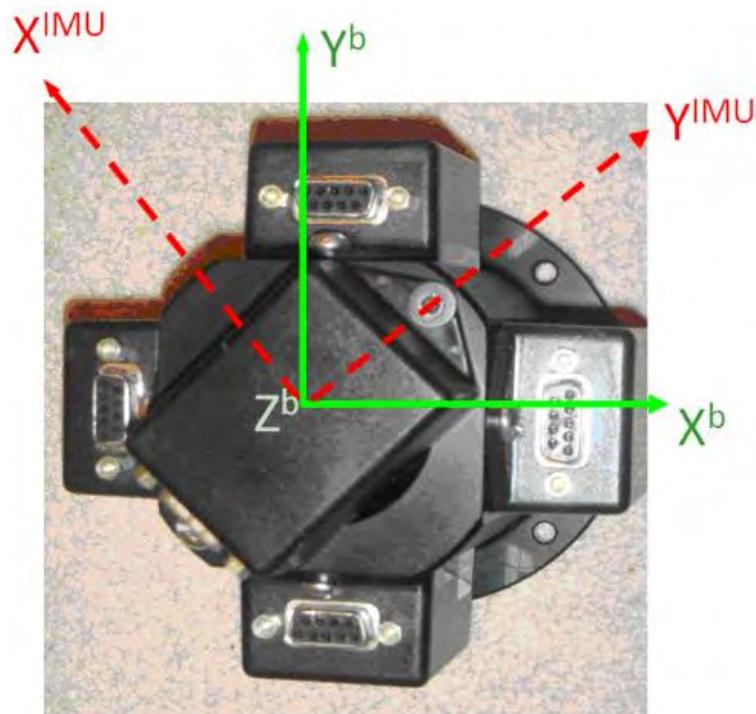testing.

Figure 3.3: Body frame in GFIMU

The body frame of the GFIMU was chosen as shown in Figure 3.3 with the z-axis along the axis of rotational symmetry coming out of the plane and with the x and y axes through the side faces of the plastic block. The origin of the frame was chosen one-fifth of distance from the plane of the centers of the four coplanar IMUs to the center of the upper IMU (Williams et al 2009). This choice of the origin is optimal in the sense that specific force at the origin will be determined by all the accelerometers due to scaling as will be explained in details in Chapter 5.

It is important to calibrate the inertial sensors being used in order to obtain an initial estimate of the biases, orientations and noise present in them. Section 3.3 discusses the method for calibration of all the five Crista MEMS IMUs.

3.3 Calibration

The performance of the GPS/GFIN integrated system is mainly determined by the output characteristics of the accelerometers employed in the system to bridge GPS outages. The output characteristics of the accelerometers are, however, dependent on their errors. Calibration of an IMU is a procedure for estimating the error models and their parameters used for sensor error compensation.

As was mentioned in Section 2.2.3, an accelerometer output can deviate from its correct value because of several error sources. They are biases, scale factor, non-orthogonality errors and noise.

In this work, a specifically designed calibration bench was used for the calibration of multiple IMUs in a GFIMU. It is used to determine the true directions of the accelerometers along with biases and scale factor errors. The estimated biases are not considered very useful as the biases of MEMS accelerometers vary substantially over time and from turn-on to turn-on. Therefore, the biases are also estimated in the Kalman filter (Section 3.6). The accelerometer orientation estimation is useful because, as mentioned previously, even a minor misalignment error of 0.1 deg can propagate an angular error of approximately 30 deg and a position error of 0.6 m in four seconds (Giansanti et al 2003).

The calibration bench used in this work is shown in Figure 3.4. It is constructed from aluminum for this purpose and manufactured to high specifications allowing rotations about two axes – horizontally and vertically. The horizontal rotation is about the circular

plate which allows rotation (*φ*) of 360º with 15º increments. Similarly, the vertical rotation is around the rectangular plate through an angle *θ* ∈ {0º, 15º……, 360º}.
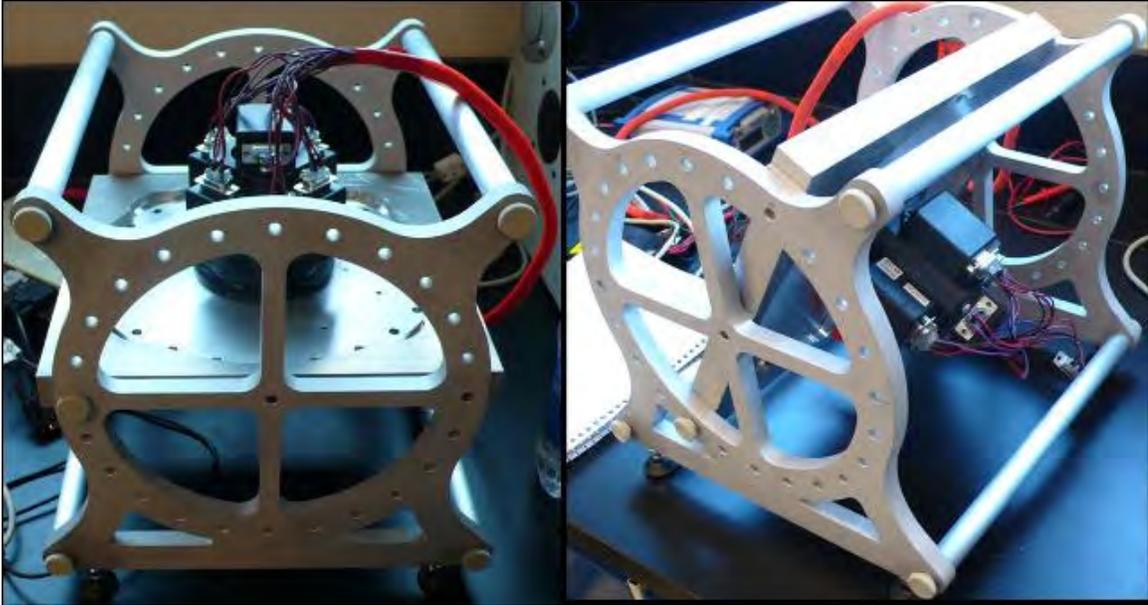

Figure 3.4: Calibration Bench

The bench was kept on a leveled plane while the data was collected, so that when *θ* was zero, the local gravity vector was orthogonal and exactly opposite to the z-axis of the body frame (Figure 3.3). For the test, static data was collected for all the IMUs for both the horizontal and vertical rotations of {0º, 45º, 90º, 135º, 180º} and {0º, 60º, 90º, 180º, 240º} respectively. For each horizontal rotation, data was collected by rotating the plate vertically, through all five rotations, thus adding up to 125 data sets. Duration of each data set was approximately 5 min and the mean was used as a measurement. The measurement of the ith accelerometer can be expressed by the equation

$$\tilde{f}_{i(j,k)} = \mathbf{v}_i^T \mathbf{R}\big(\theta_j, \varphi_k\big) f_{i(j,k)} + b_i \tag{3.1}$$

where *j* and *k* denote the different horizontal and vertical rotations

$\tilde{f}$ is the measured specific force by the accelerometer,

f is the true specific force,

$\mathbf{v}_i$ is the vector pointing in the direction of the ith accelerometer in the body frame with magnitude equal to the *gain*, as it incorporates the effect of the scale factor error,

$\mathbf{R}\left(\theta_j, \varphi_k\right)$ is the rotation matrix from the calibration bench frame to the body frame of the GFIMU. The calibration bench frame is defined in such a way that $\mathbf{R}(0,0) \equiv I$, and

b is the bias.

Collecting measurements for different θ and φ allows the solution of $\mathbf{v}_i$ and b_i in the least squares sense. The direction of the accelerometers can be found by normalizing $\mathbf{v}_i$ in the body frame.

The largest discrepancy between the assumed and calculated direction of an accelerometer axis is 1.8°. This can be because of accelerometer chip placement in casing or/and misalignment of axis on chip itself (Williams et al 2009). These calculated orientations of the accelerometers are accounted before the GFIN mathematical calculation explained in the next section.

3.4 GFIN Theory and Mathematical Computations

The basic equation for the operation of a GFIMU is the rigid body kinematic equation (Kane & Levinson 1985):

$$\mathbf{a}_P = \mathbf{a}_O + \left(\mathbf{\alpha} \times \mathbf{r}_{P/O}\right) + \mathbf{\omega} \times \left(\mathbf{\omega} \times \mathbf{r}_{P/O}\right) \qquad (3.2)$$

where $\mathbf{a}_X$ is the acceleration at point $X \in b$-frame,

$\mathbf{\alpha}$ is the angular acceleration vector of body,

$\mathbf{r}_{P/O}$ is the position vector of point P relative to O in the b-frame, and

$\mathbf{\omega}$ is the angular velocity of the body.

This equation relates the acceleration between two points P and O in the b-frame. This also incorporates the tangential and centripetal accelerations.

For the understanding of the operation of a GFIMU, it has been assumed that 'O' is the center of the body and Equation (3.2) is expressed in the b-frame. The following discussion follows closely from Williams et al (2009). From Equation (3.2), if there is a tri-axial accelerometer at point P, then ideally its output would be

$$\mathbf{f}_P = \mathbf{f}_O + \left(\mathbf{\alpha} \times \mathbf{r}_{P/O}\right) + \mathbf{\omega} \times \left(\mathbf{\omega} \times \mathbf{r}_{P/O}\right). \qquad (3.3)$$

This can be written as

$$\mathbf{f}_P = \mathbf{f}_O + \mathbf{S}(\mathbf{\alpha})\mathbf{r}_{P/O} + \mathbf{S}(\mathbf{\omega})\mathbf{S}(\mathbf{\omega})\mathbf{r}_{P/O} \qquad (3.4)$$

where

$$\mathbf{S}(\mathbf{v}) = \begin{bmatrix} 0 & -v_z & v_y \\ v_z & 0 & -v_x \\ -v_y & v_x & 0 \end{bmatrix} \qquad (3.5)$$

for any 3×1 vector $\mathbf{v}$ with i^{th} component, v_i.

Equation (3.3) can be reduced to:

$$\mathbf{f_P} = \mathbf{M_P}\zeta \tag{3.6}$$

where

$$\mathbf{M_P} = \begin{bmatrix} \mathbf{I} & -\mathbf{S}(\mathbf{r}_{P/O}) & \mathbf{X}(\mathbf{r}_{P/O}) \end{bmatrix} \tag{3.7}$$

is the *configuration matrix*, with

$$\mathbf{X}(\mathbf{r}) = \begin{bmatrix} 0 & -r_x & -r_x & r_y & r_z & 0 \\ -r_y & 0 & -r_y & r_x & 0 & r_z \\ -r_z & -r_z & 0 & 0 & r_x & r_y \end{bmatrix} \tag{3.8}$$

and

$$\zeta = \begin{bmatrix} \mathbf{f_O} \\ \alpha \\ \mathbf{qu}(\omega) \end{bmatrix} \tag{3.9}$$

where,

$$\mathbf{qu}(\omega) = \begin{bmatrix} \mathbf{sq}(\omega) \\ \mathbf{cr}(\omega) \end{bmatrix} = \begin{bmatrix} \omega_x^2 \\ \omega_y^2 \\ \omega_z^2 \\ \omega_x\omega_y \\ \omega_x\omega_z \\ \omega_y\omega_z \end{bmatrix} \tag{3.10}$$

with $\mathbf{sq}(\omega)$ and $\mathbf{cr}(\omega)$ being 3×1 matrices suggestive of *squared* and *cross* terms, respectively.

Now, if there are n tri-axial accelerometers attached to the body, then their measurements, $\mathbf{F}$, would be a $3n \times 1$ vector, and the configuration matrix $\mathbf{M}$, would be a

$3n \times 12$ matrix. Thus, for n tri-axial accelerometers, Equation (3.6) can be written in matrix product form as

$$\mathbf{F} = \mathbf{M}\zeta \tag{3.11}$$

where

$$\mathbf{M} = \begin{bmatrix} \mathbf{M}_{P_1} \\ \vdots \\ \mathbf{M}_{P_n} \end{bmatrix}. \tag{3.12}$$

The configuration matrix, $\mathbf{M}$ as can be seen from Equation (3.7) and (3.12), is fully determined by the positions of the n tri-axial accelerometers in an ideal case. Due to misalignment errors estimated by calibration as described in Section 3.3, the actual configuration matrix has a more general form which also accounts for the directions of the respective accelerometers. As $\mathbf{M}$ is a $3n \times 12$ matrix, this proves the point stated in Section 3.2, namely that at least four non-coplanar tri-axial accelerometers are required to form a GFIMU, as then $\mathbf{M}$ would be a full rank matrix of 12.

Knowing the accelerometer measurements $\mathbf{F}$ and the constant matrix $\mathbf{M}$, ζ can be determined using Equation (3.11), which comprises the specific force at point O of the body $\mathbf{f_O}$, the angular acceleration $\boldsymbol{\alpha}$ and square and cross product elements of the angular velocity $\mathbf{qu}(\boldsymbol{\omega})$. This is possible by taking the left pseudo-inverse of $\mathbf{M}$, denoted by $\mathbf{N}$:

$$\zeta = \mathbf{N}\mathbf{F}. \tag{3.13}$$

$\mathbf{N}$ will be a $12 \times 3n$ matrix and can be partitioned into four $3 \times 3n$ matrices:

$$N = \begin{bmatrix} N_f \\ N_\alpha \\ N_{sq(\omega)} \\ N_{cr(\omega)} \end{bmatrix}.$$

(3.14)

The last two matrices can be combined to make a $6 \times 3n$ matrix, $N_{qu(\omega)}$. Therefore, from Equation (3.13),

$$f_O = N_f F$$

(3.15)

$$\alpha = N_\alpha F$$

(3.16)

$$qu(\omega) = N_{qu(\omega)} F.$$

(3.17)

Thus from Equation (3.15) to (3.17), the specific force at the center of the body along with angular acceleration and $qu(\omega)$ can be determined. These angular estimates can then be used to determine the angular velocity ω, which can be determined by either integrating α from a known initial angular velocity or from $qu(\omega)$. Even when using $qu(\omega)$ estimate to determine the angular velocity, there are some problems. First, there is ambiguity since, if ω is a solution, then so is $-\omega$. Therefore, it is not possible to choose the correct solution between the two, because choosing the wrong sign may divert the estimation scheme. Also since initial angular velocity is unknown, the angular velocity estimate diverges; thus, there is an initialization problem.

It is worth mentioning here that Equation (3.15) to (3.17) relate to the causes of the disadvantages of the GFIMU pointed out in Section 3.1.1. The angular velocity ω is estimated by integrating α, hence leading to increase in errors with respect to time and

secondly, due to a pre-multiplication by a factor $\mathbf{N}_\alpha$ or $\mathbf{N}_{\mathbf{qu}(\omega)}$, the noise is more in the angular estimate as compared to the accelerometer measurements. This amplification in the disturbing effects can be explained by two different approaches. The first approach is by taking the norms of the sub-matrices of $\mathbf{N}$ described in Equation (3.14). The second approach is by taking their matrix product of the form $\mathbf{N_X N_X^T}$. The spectral norm of a matrix is the maximum singular value of the matrix. It is directly related to the amount of error amplification in the angular estimates. Similarly, the product $\mathbf{N_X N_X^T}$, directly relates to the noise in the accelerometer measurements that is propagated to the angular estimates. These approaches will be used when discussing the results in Chapter 5. The application of these amplification measures, operation of a GFIMU and different causes for the disadvantages in a GFIMU can be more easily understood by considering the case of a planar motion. Figure 3.5 shows the planar case of a GFIMU.
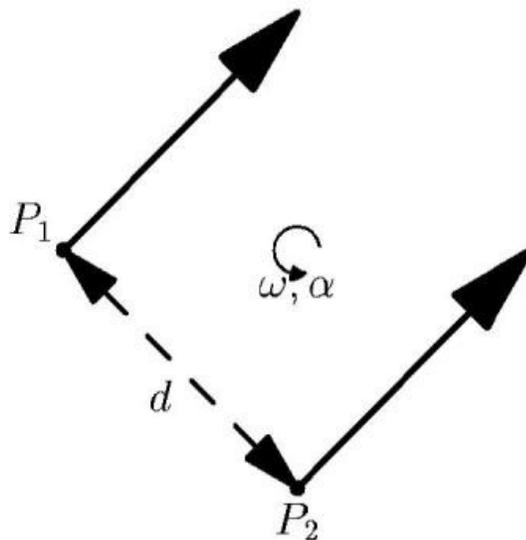

Figure 3.5: Planar GFIMU (Williams et al 2009)

Suppose there is a parallel pair of accelerometers kept at points P_1 and P_2 separated by a vector orthogonal to their directions. The angular acceleration α can be estimated by weighted differencing of the accelerometer measurements given by

$$\alpha = \underbrace{\frac{1}{d}\begin{bmatrix} -1 & 1 \end{bmatrix}}_{\mathbf{N}_\alpha} \underbrace{\begin{bmatrix} f_{P_1} \\ f_{P_2} \end{bmatrix}}_{\mathbf{F}} \text{ or } \alpha = \frac{f_{P_2} - f_{P_1}}{d}. \tag{3.18}$$

A similar equation can be written to estimate ω^2. It can be seen from Equation (3.18), that the errors and noise in the α estimate will be proportional to the specific force measurements. The maximum error in the GFIMU estimate of α is bounded as follows:

$$\left\| \hat{\alpha}_{GFIMU} - \alpha \right\|_2 \le \left\| \mathbf{N}_\alpha \right\|_2 \left\| \mathbf{b_a} + \mathbf{\eta_a} \right\|_2 \tag{3.19}$$

where $\left\| \mathbf{N}_\alpha \right\|_2$ denotes the spectral norm of $\mathbf{N}_\alpha$, and $\mathbf{b_a}$ and $\mathbf{\eta_a}$ denote the accelerometer bias and noise, respectively.

For the above planar case, the spectral norm $\left\| \mathbf{N}_\alpha \right\|_2$ will be $\frac{\sqrt{2}}{d}$, thus for $d = 5$ cm, it would be equal to 28.28. This indicates that the ratio of magnitude of the error in the GFIMU estimate of α to the error in the accelerometer measurements can be up to 28.28. The second approach to quantify the error magnification just takes the accelerometer measurement noise into account:

$$\hat{\alpha}_{GFIMU} - \alpha = \mathbf{N}_\alpha \mathbf{\eta_a}. \tag{3.20}$$

Suppose the covariance matrix of $\mathbf{\eta_a}$ is $\mathbf{Q_a} = \rho^2 \mathbf{I}$, where ρ^2 is the noise variance of each accelerometer and it is assumed that there is negligible correlation between the accelerometer noise variance. Therefore, the variance of error in the estimate of α is

$$\mathbf{N}_\alpha \mathbf{Q_a} \mathbf{N}_\alpha^T = \rho^2 \mathbf{N}_\alpha \mathbf{N}_\alpha^T = 2\frac{\rho^2}{d^2}. \tag{3.21}$$

For $d = 5$ cm, the variance of the α estimate would be 800 times variance of noise affecting the two accelerometer measurements, and if d is larger suppose, 5 m, the variance become 0.08 times. Thus, the distance between the accelerometers is crucial for error propagation in the angular estimates α and ω^2. For spatial (3D) accelerometer configurations, the same general result holds: the smaller the configuration, the more the errors of the accelerometers is magnified in the estimates of the angular motion. Moreover, when $\boldsymbol{\omega}$ is estimated, the noise amplification may mask the original motion of the body in low dynamic situations.

3.5 GFIN+ Concept and Theory

Having discussed the problems with a GFIMU, this section presents the proposed approach of the GFIN+. This is a compromise between GFIN and traditional Strapdown Inertial Navigation systems. A single MEMS-IMU based INS integrated with GPS is termed a strapdown inertial navigation system in this work. Inertial navigation is used with GFIMU instead of pedestrian dead reckoning (PDR), because pedestrians use different modes of navigation, for example walking mode, vehicle mode etc. Therefore, PDR cannot be used at all times as it depends on step length detection and estimation. Thus, in this work GFIN is used as it provides a navigation solution in any mode of navigation.

In this work, a single tri-axial gyroscope is added to the GFIMU in order to mitigate the problems discussed in Section 3.4. The gyroscope can be used to initialize the angular velocity estimate which will help with the faster convergence of the solution and keep the error in bounds. It is useful especially when the angular acceleration and $\mathbf{qu}(\omega)$ estimates are of poor quality, i.e. having large errors in low dynamic situations. Consequently, this gyroscope addition can be thought as a GFIMU aiding the GPS/MEMS-INS integration. This aiding by a GFIMU can potentially improve the performance of a traditional MEMS based SIN system in estimates of specific force. This is because more accelerometers are being used, therefore, averaging the noise. Also, if the gyroscope is of poor quality or in situations of higher angular dynamics, where the gyroscope might not be reliable because of limited angular dynamic range, a GFIMU will have better performance. Figure 3.6 shows the block diagram of the proposed approach. The gyroscope measurements are combined with GFIMU measurements in a GFIN+ EKF (Section 3.6) to give the angular velocity estimate and the accelerometer biases estimates. These bias estimates can be used to correct the GFIMU measurements, which are then pre-multiplied by the multiplication factor $\mathbf{N_f}$, thus getting the specific force estimates of the body. These outputs can then be used as virtual IMU measurements and integrated with GPS using tightly-coupled integration scheme. The tight integration is done using GPS/INS Integration Navigation Software (GIINS) (Godha 2006). This filter contains 15 states consisting of three states each of position, velocity, attitude, gyroscope biases and accelerometer biases.
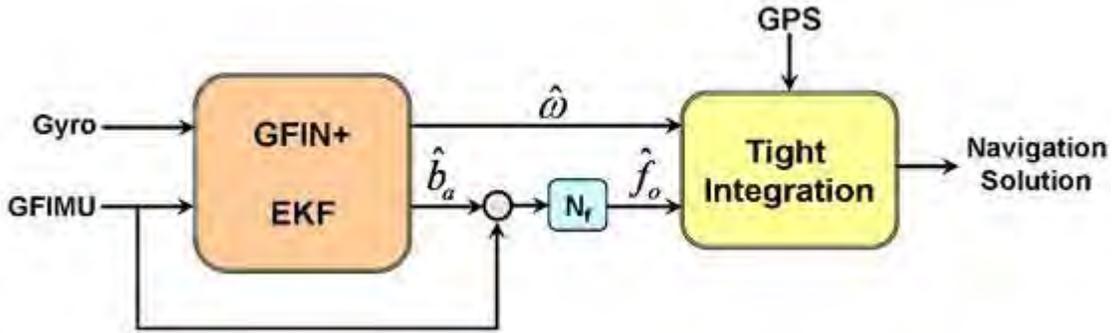
Figure 3.6: Block Diagram showing GFIN+ approach

3.6 GFIN+ Kalman Filter Design

This section discusses the internal working of the GFIN+ EKF used in this work and follows Williams et al (2009).

Suppose the measurements of the accelerometers at instant k can be expressed by a $3n \times 1$ vector $\tilde{\mathbf{F}}_k$ and the corresponding true or ideal accelerometer measurements are denoted by by $\mathbf{F}_k$, then according to Equation (2.23), they can be related as

$$\tilde{\mathbf{F}}_k = \mathbf{F}_k - \mathbf{b}_{\mathbf{a}_k} - \mathbf{\eta}_{\mathbf{a}_k} \tag{3.22}$$

where $\mathbf{b}_\mathbf{a}$ is a $3n \times 1$ vector representing the accelerometer biases,

$\mathbf{\eta}_\mathbf{a}$ is a $3n \times 1$ vector representing the accelerometer white noise sequences with diagonal and constant covariance matrix, $\mathbf{Q}_\mathbf{a}$.

The accelerometer biases $\mathbf{b}_\mathbf{a}$ are expressed as Gauss Markov (GM) sequences:

$$\mathbf{b}_{\mathbf{a}_{k+1}} = e^{-D(\beta_\mathbf{a})\Delta t}\mathbf{b}_{\mathbf{a}_k} + \mathbf{\eta}_{\mathbf{b}_{\mathbf{a}_k}} \tag{3.23}$$

where β_a is a $3n \times 1$ vector representing the reciprocals of time constants of the biases of

accelerometers

$D(X)$ represents the diagonal matrix $3n \times 3n$ of a $3n \times 1$ vector X,

η_{b_a} is the $3n \times 1$ white noise vector with covariance matrix $\mathbf{Q}_{b_a}$, and

Δt is the sample interval.

Similarly, the gyroscope measurements can be based on Equation (2.24) and at an instant

k can be expressed by the equation

$$\tilde{\omega}_k = \omega_k - \mathbf{b}_{g_k} - \eta_{g_k} \tag{3.24}$$

where $\tilde{\omega}$ is the 3×1 vector of tri-axial gyroscope measurements,

ω is the 3×1 vector of ideal tri-axial gyroscope measurements,

η_g is a 3×1 vector of white noise with a constant and diagonal covariance matrix

$\mathbf{Q}_g$,

$\mathbf{b}_g$ is a 3×1 vector of Gauss Markov sequences similar to Equation (3.23) which

can be written as

$$\mathbf{b}_{g_{k+1}} = e^{-D(\beta_g)\Delta t}\mathbf{b}_{g_k} + \eta_{b_{g_k}} \tag{3.25}$$

where the parameters mean the same as described above but for gyroscope instead of

accelerometer. The noise covariance matrix for the gyroscope bias is denoted by $\mathbf{Q}_{b_g}$.

3.6.1 State-Space Model

A discrete-time state space model combining the measurements of the GFIMU and the tri-axial gyroscope is now presented. The state is assumed to be the following $(6 + 3n) \times 1$ vector which comprises of the angular velocity of the body ($\boldsymbol{\omega}$), the gyroscope biases ($\mathbf{b}_\mathbf{g}$), and the accelerometer biases ($\mathbf{b}_\mathbf{a}$):

$$\mathbf{x}_k = \begin{bmatrix} \boldsymbol{\omega}_k \\ \mathbf{b}_{\mathbf{g}_k} \\ \mathbf{b}_{\mathbf{a}_k} \end{bmatrix}. \tag{3.26}$$

Angular accelerations are not included in the state but are used to propagate the angular velocity estimate:

$$\boldsymbol{\omega}_{k+1} = \boldsymbol{\omega}_k + \boldsymbol{\alpha}_k \Delta t. \tag{3.27}$$

This is advantageous as the size of the state does not need to be increased and no stochastic model is needed for $\boldsymbol{\alpha}$ as it would have to be changed according to the specific applications. Therefore, from Equations (3.23), (3.25), and (3.27), the state vector at instant *k+1* can be written as

$$\mathbf{x}_{k+1} = \begin{bmatrix} \boldsymbol{\omega}_k + \boldsymbol{\alpha}_k \Delta t \\ e^{-D(\boldsymbol{\beta}_\mathbf{g})\Delta t} \mathbf{b}_{\mathbf{g}_k} + \boldsymbol{\eta}_{\mathbf{b}_{\mathbf{g}k}} \\ e^{-D(\boldsymbol{\beta}_\mathbf{a})\Delta t} \mathbf{b}_{\mathbf{a}_k} + \boldsymbol{\eta}_{\mathbf{b}_{\mathbf{a}k}} \end{bmatrix}. \tag{3.28}$$

Substituting $\boldsymbol{\alpha}$ from Equation (3.16) into Equation (3.28), the following discrete-time state equation can be obtained:

$$\mathbf{x}_{k+1} = \mathbf{A}\mathbf{x}_k + \mathbf{B}\tilde{\mathbf{F}}_k + \mathbf{w}_k \tag{3.29}$$

with

$$\mathbf{A} = \begin{bmatrix} \mathbf{I} & \mathbf{0} & \mathbf{N}_\alpha \Delta t \\ \mathbf{0} & e^{-D(\beta_g)\Delta t} & \mathbf{0} \\ \mathbf{0} & \mathbf{0} & e^{-D(\beta_a)\Delta t} \end{bmatrix} \tag{3.30}$$

$$\mathbf{B} = \begin{bmatrix} \mathbf{N}_\alpha \Delta t \\ \mathbf{0} \\ \mathbf{0} \end{bmatrix} \tag{3.31}$$

$$\mathbf{w}_k = \begin{bmatrix} \mathbf{N}_\alpha \Delta t \boldsymbol{\eta}_{\mathbf{a}_k} \\ \boldsymbol{\eta}_{\mathbf{b}_{g_k}} \\ \boldsymbol{\eta}_{\mathbf{b}_{a_k}} \end{bmatrix} \tag{3.32}$$

The covariance matrix of the process noise $\mathbf{w}_k$ is denoted by $\mathbf{Q}$ and given by

$$\mathbf{Q} = \begin{bmatrix} (\Delta t)^2 \mathbf{N}_\alpha \mathbf{Q}_\mathbf{a} \mathbf{N}_\alpha^T & \mathbf{0} & \mathbf{0} \\ \mathbf{0} & \mathbf{Q}_{\mathbf{b}_g} & \mathbf{0} \\ \mathbf{0} & \mathbf{0} & \mathbf{Q}_{\mathbf{b}_a} \end{bmatrix} \tag{3.33}$$

3.6.2 Measurement Model

The measurements available at the kth instant are those of the tri-axial gyroscope and the GFIMU estimates of the quadratic combinations of the components of the angular velocity vector, $\mathbf{qu}(\boldsymbol{\omega})$ (Equation (3.17)). Thus, the measurement equation can be written as

$$\mathbf{z}_k = \begin{bmatrix} \tilde{\boldsymbol{\omega}}_k \\ \mathbf{N}_{\mathbf{qu}(\boldsymbol{\omega})} \tilde{\mathbf{F}}_k \end{bmatrix}. \tag{3.34}$$

This equation can be re-written in the Kalman filter measurement equation form as

$$\mathbf{z}_k = \mathbf{h}(\mathbf{x}_k) + \mathbf{v}_k \qquad (3.35)$$

where $\mathbf{x}_k$ is the state vector at instant k defined by Equation (3.26), with

$$\mathbf{h}(\mathbf{x}_k) = \begin{bmatrix} \boldsymbol{\omega}_k - \mathbf{b}_{\mathbf{g}_k} \\ \mathbf{qu}(\boldsymbol{\omega}_k) - \mathbf{N}_{\mathbf{qu}(\omega)} - \mathbf{b}_{\mathbf{a}_k} \end{bmatrix} \qquad (3.36)$$

$$\mathbf{v}_k = \begin{bmatrix} -\boldsymbol{\eta}_{\mathbf{g}_k} \\ -\mathbf{N}_{\mathbf{qu}(\omega)}\boldsymbol{\eta}_{\mathbf{a}_k} \end{bmatrix}. \qquad (3.37)$$

The measurement noise covariance matrix can be estimated as

$$\mathbf{R} = \begin{bmatrix} \mathbf{Q}_{\mathbf{g}} & \mathbf{0} \\ \mathbf{0} & \mathbf{N}_{\mathbf{qu}(\omega)}\mathbf{Q}_{\mathbf{a}}\mathbf{N}_{\mathbf{qu}(\omega)}^{T} \end{bmatrix}. \qquad (3.38)$$

According to Brown & Hwang (1997), correlation between process noise at instant *k-1*, $\mathbf{w}_{k-1}$ and measurement noise at instant *k*, $\mathbf{v}_k$, is important. Since accelerometer noise $\boldsymbol{\eta}_{\mathbf{a}}$ is common between the two and since it is a white sequence, the two matrices should be uncorrelated.

Chapter Four: De-noising Inertial Sensor Signals: Wavelet Analysis

This chapter provides an introduction to the methods which can be used for de-noising MEMS-based inertial sensors. Two methods are considered: Wavelets and Low pass filtering. First, the frequency spectrum of the inertial sensor measurements is discussed. This provides an insight into the frequency distribution of noise present in inertial sensors. This is followed by a discussion of the wavelet transform and wavelet multi-resolution analysis (WMRA), which is an analysis of the signal at different frequencies with different resolutions. WMRA is implemented to reduce the noise in the sensor signals. After this, de-noising via low pass filtering is discussed. The noise and the sensor errors that are mixed with motion dynamics are removed, and more reliable data is provided to the Kalman filter based GPS/INS integration module (Hamid 2005).

4.1 INS Error Bandwidth

Before discussing the wavelet method, it is important to understand the frequency spectrum of the IMU measurements. Figure 4.1 shows the frequency spectrum plot exhibited by an IMU. As can be seen from Figure 4.1(a), the errors in inertial sensors are a combination of two types of errors, (1) the short-term, high frequency errors, and (2) the long-term, low frequency errors. The long term errors are reduced by GPS/INS integration, as GPS measurements update the Kalman filter. The short term errors are partially reduced by smoothing which results from the numerical integration process of the INS mechanization (Hamid 2005). Smoothing occurs since the inertial sensor data

rate is 100 Hz while the INS output rate is 10-20 Hz which leads to accumulation of data and hence, averages out some of the noise. Figure 4.1 (b) shows the residual error after the INS mechanization and GPS/INS integration. To reduce the remaining short-term errors, de-noising methods based on wavelets or low pass filtering can be used.
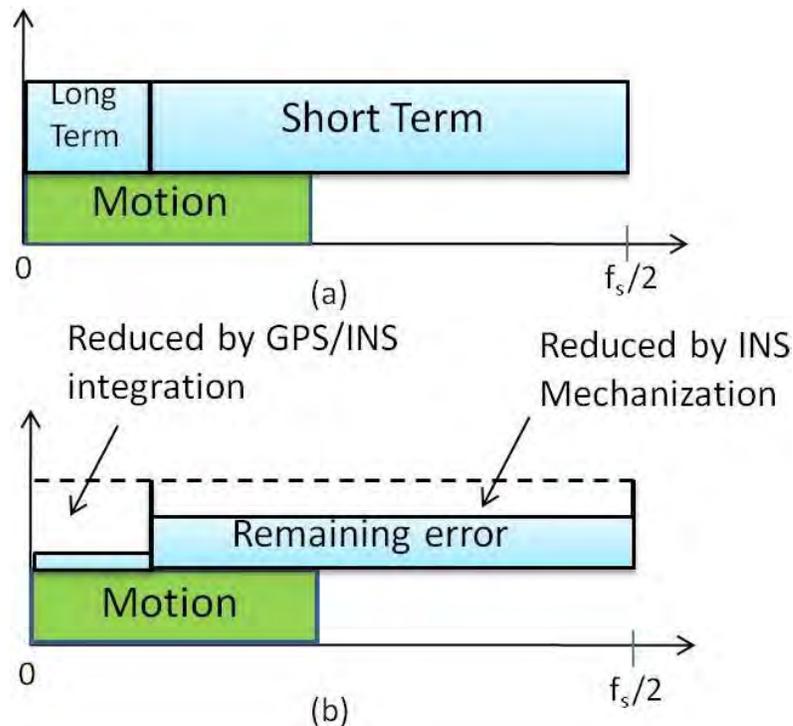

Figure 4.1: Frequency Spectrum of an IMU (a) Raw Measurements (b) After Standard Processing (f_s is sampling frequency) (Adapted from Bruton et al 99, Hamid 05)

The consideration of the frequency spectrum of inertial sensor signals is quite beneficial to verify the theoretical plot. The Fourier transform is plotted for both static and kinematic accelerometer and gyroscope data. Interpretation of this spectrum helps in recognizing the frequency bands of the signals of interest representing the actual motion and the disturbing sequence of noise. Figure 4.3 and Figure 4.4 show the spectrum of Crista MEMS X-accelerometer output, in static and kinematic modes respectively. The

kinematic mode considered in this section corresponds to the case when an accelerometer is rigidly mounted on a plank and given rotations about all axes of the body frame as shown in Figure 4.2.
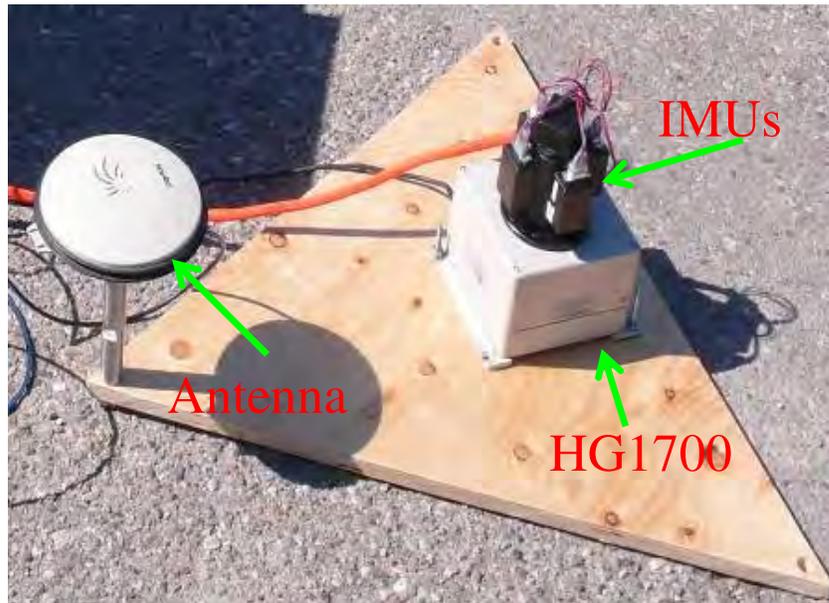

Figure 4.2: Kinematic mode: IMU attached to the wooden plank

For both the static and kinematic cases the noise is distributed throughout the entire frequency range. In the kinematic case, it can be seen that the motion of interest is in a low frequency band of approximately 0.5 to 1 Hz when the IMU is in hand. This band changes accordingly when the IMU is placed on a foot or on the back. Since the foot experiences more rotation the frequency band of motion increases to approximately 5-10 Hz. This is used as the cut-off frequency for low pass filtering.
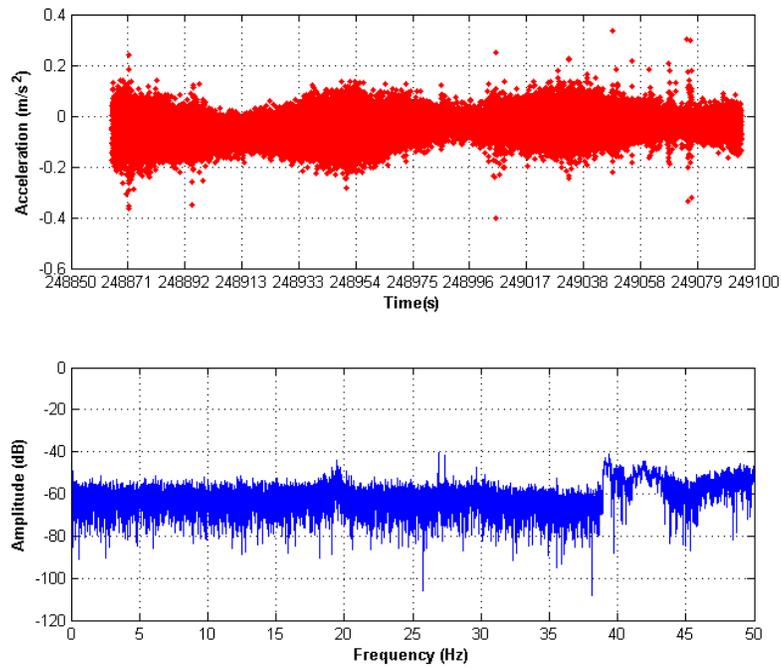
Figure 4.3: Frequency Spectrum of measurements of a Stationary MEMS accelerometer
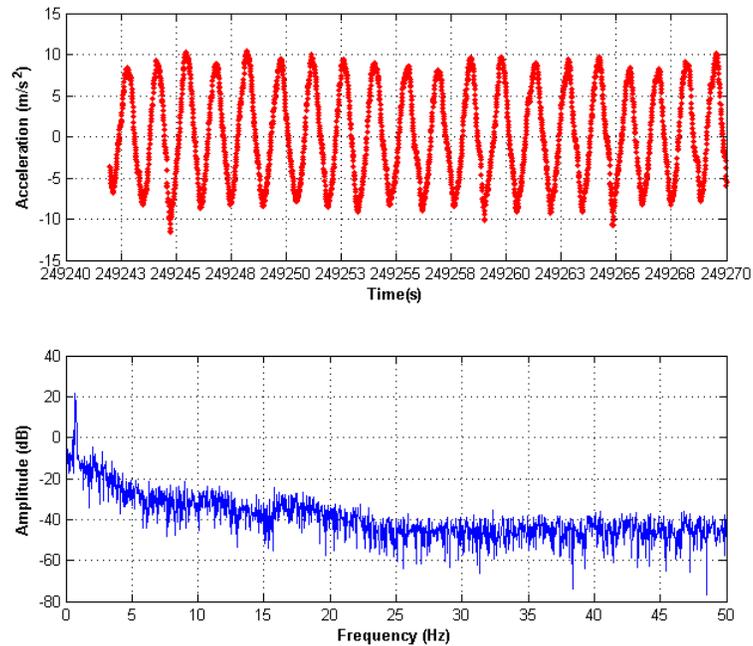

Figure 4.4: Frequency Spectrum of measurements of a Kinematic MEMS accelerometer

Figure 4.5 and Figure 4.6 show the frequency spectrums of the measurement of a Crista MEMS gyroscope in static and kinematic modes respectively. Again the same observation is made, as noise is distributed over the whole frequency range. The actual signal has zero frequency in static mode. In kinematic mode the motion of interest is in the range of 0.5 – 4 Hz. Thus, these plots verify the theoretical plot of frequency spectrum shown in Figure 4.1, indicating that the motion of interest is in a low frequency band. Therefore, the errors or noise can be removed either by low pass filtering or by using wavelet de-noising. It has been shown (Skaloud 99) that wavelet de-noising also allows the removal of noise and vibrations which overlaps the signal of interest.
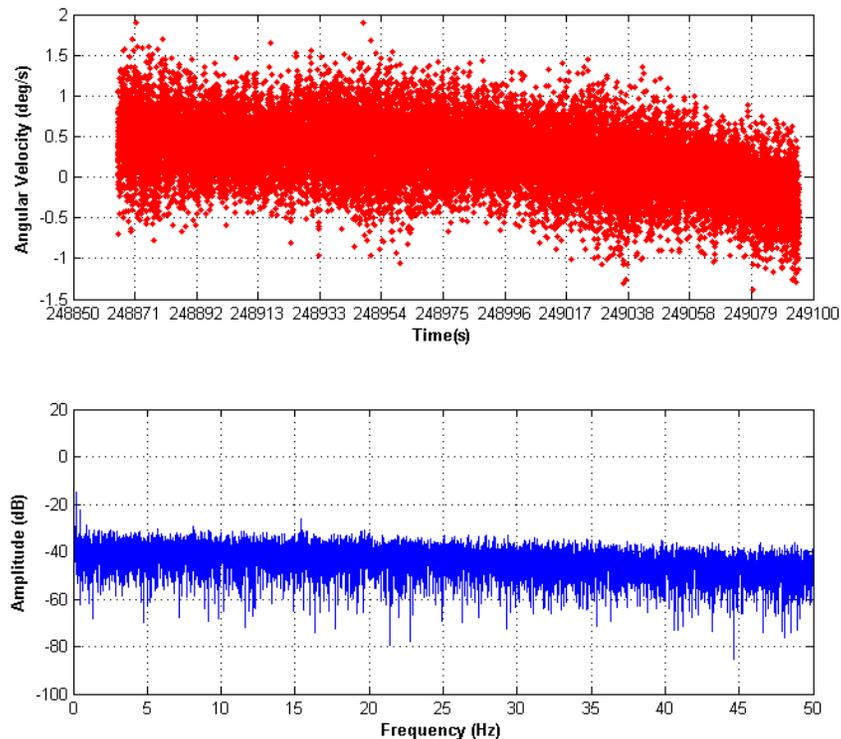

Figure 4.5: Frequency Spectrum of measurements of a MEMS gyroscope in static mode
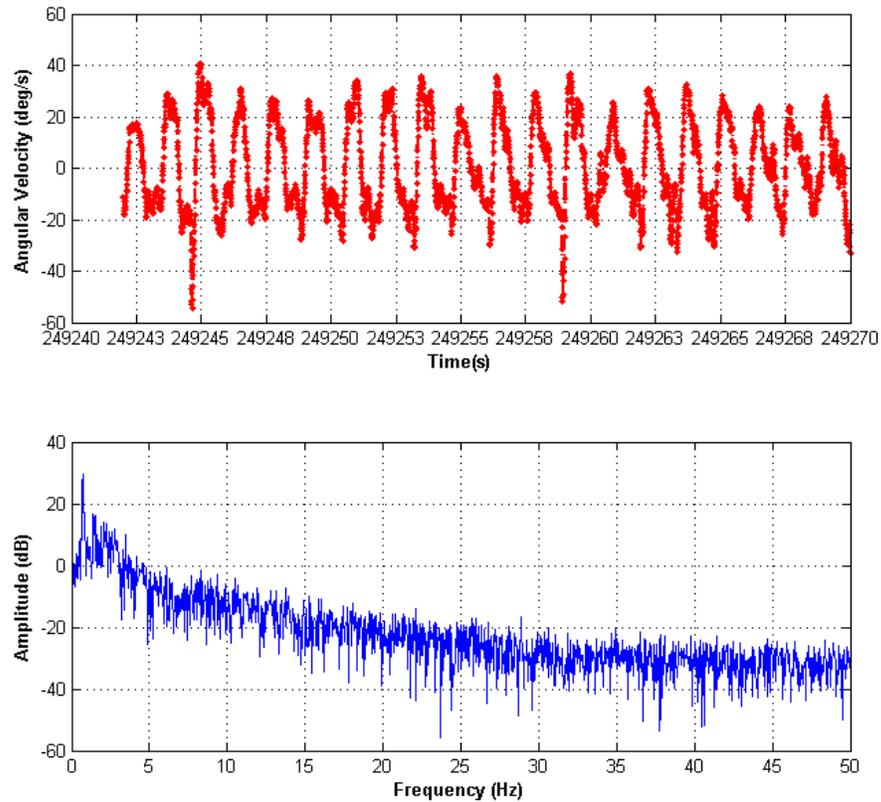
Figure 4.6: Frequency Spectrum of measurements of a MEMS gyroscope in kinematic mode

4.2 Wavelets and Wavelet Transform

Wavelets are mathematical functions that separate the data into different frequency components and analyse each component with different resolutions (Graps 2004). They have received extensive attention in many fields of engineering over the last two decades leading to many applications including image compression, medical diagnostics, geophysical signal processing, turbulence prediction etc (e.g. Nassar 2003, Graps 2004). Wavelets are of interest in signal processing because of their localization properties. Wavelet techniques are based on analysing the signal through signal windowing with

variable window sizes. Thus, they have an advantage over other signal processing techniques because they can be used to analyse a localised portion of a large signal (Polikar 1996). Due to this localisation property, the wavelet technique is better than other methods like Fourier Transforms in inertial sensor signals which are of unknown smoothness i.e. with abrupt jumps, sharp spikes and other irregularities.

4.2.1 Continuous Wavelet Transform

The continuous wavelet transform (CWT) of a time domain signal x (t) is defined as (Mallat 1999)

$$CWT_x^{\psi}(\tau,s) = \Psi_x^{\psi}(\tau,s) = \frac{1}{\sqrt{|s|}} \int_{-\infty}^{\infty} x(t)\psi^*\left(\frac{t-\tau}{s}\right)dt \qquad (4.1)$$

where τ is the translation parameter,

s is the scale parameter, and

ψ is the transforming/analysing/wavelet function, also called as a mother wavelet because it is a prototype for generating different window functions which are called the daughter wavelets.

* denotes the conjugate transpose

Translation is the time information in the transformed signal and corresponds to shifting of the window through the signal. Scale indicates the wavelet's width which either dilates or compresses a signal. Large scales correspond to dilated (or stretched out) signals and small scales correspond to compressed signals thus, enabling higher frequency

information to be detected. The CWT (Equation (4.1)) gives the wavelet coefficients as a function of τ and s. The calculated coefficients refer to the closeness of the signal to the wavelet of the current scale. Thus, if the signal at one of its locations has a spectral component that is closely related to that of the wavelet at the current scale, the computed coefficient at this point will have a relatively large value and vice versa (Polikar 2006). The determination of the CWT coefficients of a signal starts by using the most compressed wavelet that can detect the highest frequencies existing in that signal. The wavelet is then shifted by τ until the end of the signal. Scale s is then increased and the same procedure is repeated again until some 'maximum' desired value of s is reached. This will result in a collection of time-scale representations of the signal, all with different resolutions and so one can have a multi-resolution analysis or the WMRA (Valens 2004).

To summarize, the wavelet transform of a time domain signal can be defined as a projection of a signal onto a family of basis functions that are generated by dilations (or compressions) and translations of a single mother wavelet.

Mother wavelets are not limited to complex exponential or sinusoidal functions, as is the case of Fourier transform, but they need to fulfill some properties: e.g. be oscillatory, decay and tend to zero with an increase of distance (Elhabiby 2007). These restrictions are required so that the integration of the Equation (4.1) is finite (Hamid 2005). The selection of mother wavelets is discussed in Section 4.4.

4.2.2 Discrete Wavelet Transform

The CWT operates at every scale from that of the original signal up to some maximum scale which can be determined by trading off the need for detailed analysis with available computational power. It is also continuous in terms of shifting, as the analyzing wavelet is shifted smoothly over the full domain of the analyzed function (Misiti 2009). The discrete wavelet transform (DWT) provides sufficient information both for analysis and synthesis of the original signal, with a significant reduction in the computation time as compared to CWT. The DWT uses discrete values of scale (*s*) and translation (τ) parameters which depend on a constant number, α (Equation (4.2). Thus, the DWT evaluates the coefficients at specific scales and translations unlike that of CWT which computes the coefficients for every possible scale and helps in reducing the redundancy in CWT. The sampling of s and τ in DWT takes the form (Nassar 2003)

$$s = \alpha^m$$
$$\tau = m\alpha^n \tag{4.2}$$

where *m* and *n* are the dilation and translation indices. Generally, wavelet bases with α = 2 are used (ibid). By substituting Equation (4.2) in Equation (4.1), one obtains

$$CWT_x^{m,n} = \frac{1}{\sqrt{\alpha^n}} \int_{-\infty}^{\infty} x(t)\psi\left(t\alpha^{-n} - m\right) dt \tag{4.3}$$

Discretizing x (t) to x (k) and assuming a sampling rate of 1 with α = 2, the DWT of a discrete time signal x (k) can be described by two integers m and n as

$$DWT_x^{m,n} = \frac{1}{\sqrt{2^n}} \sum_k x(k)\psi\left(k\,2^{-n} - m\right) \tag{4.4}$$

The DWT is implemented based upon a bank of discrete-time filters that have half-band low-pass and high-pass characteristics. A half-band low-pass filter is a filter that removes all frequencies that are above half of the highest frequency in the signal. The wavelet coefficients are computed by passing the signal through two complementary filters, low pass (LP) and high pass (HP) filters. This leads to the decomposition of the input signal into two parts: approximation and details. The output from the low pass filter is called the approximation, which is of interest as it comprises mainly the signal identity. Similarly, the high frequency component, the details part, is mainly constituted of noise (see Figure 4.7). To reconstruct a signal from the approximation and details part the Inverse Discrete Wavelet Transform (IDWT) is used which is given by the following equation:

$$x(k) = \sum_m \sum_n \frac{1}{\sqrt{2^n}} DWT_x^{m,n} \psi^*\left(k\, 2^{-n} - m\right) \tag{4.5}$$

4.3 Wavelet Multi-Resolution Analysis

As explained in the previous section, the inertial sensor signal is decomposed into two parts: approximation and details. WMRA is analysing the signal at different frequencies with different resolutions. The wavelet decomposition is carried out till a level where almost all the noise is removed from the low frequency approximation part. This level is called the level of decomposition (LOD). This procedure of decomposition is called WMRA or wavelet multiple level of decomposition.
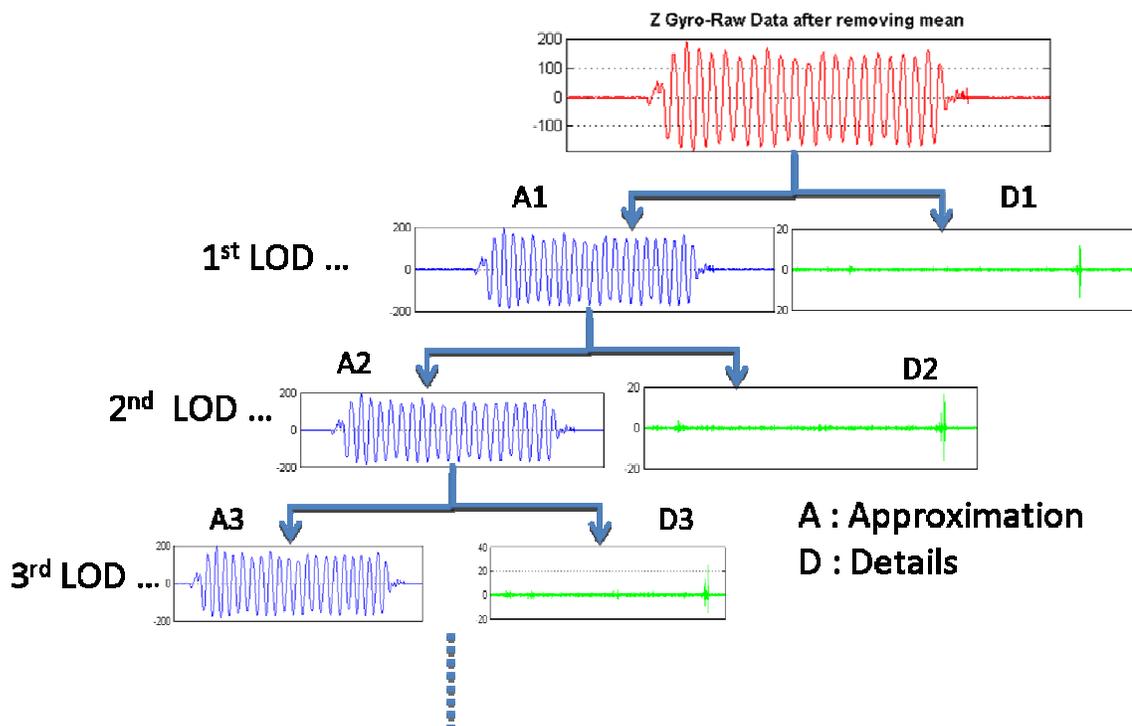
Figure 4.7: Wavelet Multi-Resolution Analysis of a Z Gyroscope data (in deg/s)

WMRA allows obtaining finer resolution frequency components of a specific signal by successive decompositions of the obtained approximation parts. This capability of representing a signal at several levels of resolution constitutes one of the major benefits of wavelets over other signal processing techniques.

4.4 Selection of Wavelet Type

There are a large number of mother wavelets available, some of which are shown in Figure 4.8. Most of the publications on applications of wavelet analysis, particularly for data compression and data de-noising, use the wavelet base which gives few non-zero

wavelet coefficients (Mallat 1999). A signal has few non-negligible wavelet coefficients if most of the detail wavelet coefficients are small. Thus, the wavelet that produces a maximum number of wavelet coefficients that are close to zero is chosen as a mother wavelet (ibid).
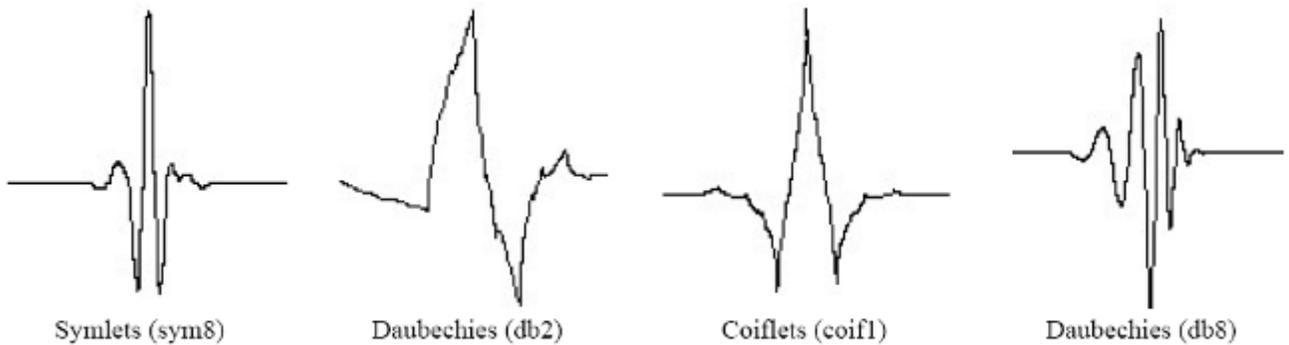

Figure 4.8: Examples of some Mother Wavelets (Nassar 2003)

The selection of a mother wavelet can be based on the study of the previous trials performed by previous researchers. In this work, the inbuilt functions of MATLAB are used for de-noising the inertial sensor signals. The wavelet type Daubechies 'db8' is used. Daubechies 'db8' has been used by a number of researchers (e.g Hamid 2005, Nassar 2003) and has proved to be useful for de-noising the inertial sensor signals.

4.5 Wavelet De-noising

The sensor signal of interest is generally in the low frequency region while the noise is spread over all the frequencies thus characterizing white noise. The wavelet de-noising method using wavelet thresholding (Section 4.5.1) has been successfully used for de-

noising the inertial sensor signals (Skaloud 1999). The wavelet de-noising method consists of three main steps:

1. Apply DWT to decompose the signal into low and high frequency components as discussed in Section 4.3.

2. Apply a thresholding technique: Soft Thresholding or Hard Thresholding (Section 4.5.1).

3. Invert the DWT to reconstruct the de-noised signal using low frequency coefficients and the modified high frequency coefficients discussed in Section 4.2.2.

4.5.1 Wavelet Thresholding

The wavelet thresholding technique was mainly developed for removing noise and outliers, compression, and pattern recognition of the signal before wavelet reconstruction (Elhabiby 2007). It was observed by Jansen (2000) that smaller coefficients are dominated by noise compared to larger coefficients that carry more signal information than noise. Thus, replacing the small, noisy coefficients by zero and applying the IDWT on the result leads to the reconstruction of the signal with less noise.

There are two thresholding methods which are generally used: Hard Thresholding and Soft Thresholding (Misiti 2009, Elhabiby 2007, Hamid 2005). Hard thresholding is the most basic way of thresholding in which any wavelet coefficient with an absolute value below a given threshold is replaced by zero. The wavelet coefficients which have an absolute value greater than the threshold are the ones which are used for the

reconstruction of the signal. Soft thresholding is an extension of hard thresholding. In this case, coefficients with absolute values lower than the threshold are set to zero, and then the non-zero coefficients are attenuated. These two thresholding methods are shown in Figure 4.9.
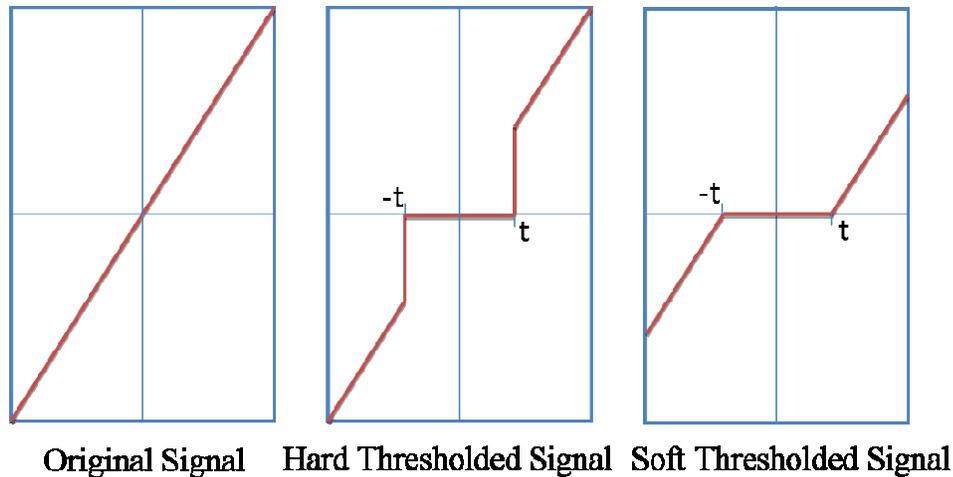

Original Signal   Hard Thresholded Signal Soft Thresholded Signal

Figure 4.9: Thresholding of signal s = x with threshold t

The equations describing the thresholding methods are:

Hard Thresholding:
$$\begin{aligned} s &= x \quad if \ |x| > t \\ s &= 0 \quad if \ |x| \le t \end{aligned}$$
(4.6)

Soft Thresholding:
$$\begin{aligned} s &= sign(x)(|x| - t) \quad if \ |x| > t \\ s &= 0 \qquad\qquad\qquad if \ |x| \le t \end{aligned}$$
(4.7)

where t is the threshold, and

$sign\ (\ )$ is the sign operator.

The choice of a threshold, t obviously has a large impact. A high threshold may result in loosing some of the signal components whereas; a low threshold will result in retaining noise in the final output. Many researchers (Elhabiby 2007, Hamid 2005, Skaloud 1999)

have proposed that the threshold t should be selected according to the standard deviation of the Gaussian noise (σ) and the length of the observations (N) as

$$t = \sigma\sqrt{2\log N}$$.
 (4.8)

The wavelet de-noising procedure is applied to real inertial sensor data and the results are discussed in Chapter 5.

4.6 Low-pass filtering De-noising

As was discussed in Section 4.1, the frequency region of interest is the low frequency band, so it seems obvious to de-noise the inertial sensor signals by passing them through a low-pass filter. The Butterworth low pass filter is an ideal choice since it treats the amplitude of the pass-band as nearly constant, in other words it has a maximally flat pass-band (Guo et al 2004). The Butterworth filter permits the amplitude error up to a scale in the pass-band which corresponds to the pass-band frequency on the frequency scale, and in the stop-band, the amplitude attenuation is larger than another scale corresponding to stop-band frequency. According to a chosen set of stop-band and pass-band frequencies, Guo et al (2004) estimated that a Butterworth low-pass filter with order 5 and cut-off frequency, f = 10 Hz is suitable for filtering the IMU heading raw data. Thus, in this work a similar filter will be used to de-noise the inertial sensor signals and verify the above mentioned work. The cut off frequency varies with the dynamics of the motion and differs in each case if GFIMU is kept on the back, in hand or on foot.

4.7 Comparison of Wavelet and Low-pass filtering De-noising

Wavelet de-noising is becoming a popular alternative to classical low pass filters, as it is particularly adapted for analysis of non-stationary signals. Non-stationary signals can be defined as those signals which are well localised in time (Dolabdjian 2002). Low pass filters present many deficiencies in analysing signals with high temporal variation and/or well localised in time due to infinite support nature of Fourier basis waveforms (i.e. sine and cosine). This leads to spreading the energy of such signals on a high number of coefficients, which makes it hard to discriminate signals from a noisy background. As discussed in Section 4.2 and 4.3, wavelet analysis possesses good localisation both in time and frequency scales. Wavelet de-noising has the advantage that signals with very sharp changes can be analysed very successfully. Secondly, low pass filtering has a disadvantage as it cannot filter the noise over the frequency band containing both signal and noise. On the other hand, low pass filtering is computationally simple and needs less computational power as compared to wavelet de-noising.

Both the de-noising methods will be used to de-noise the signals and will be compared on both the position and measurement levels, which are discussed in Chapter 5.

Chapter Five: Field Testing, Results and Analysis

This chapter quantifies the performance of a GFIMU and the integrated GFIN+ system. The chapter begins with a description of the field tests where the specific details about the test set-up, operating environment and the procedures adopted for the data collection are discussed. This is followed by the data processing methodology and the results obtained in both the measurement and position domains. The measurement domain results include the results with angular velocity and specific force levels.

5.1 Field Test Description

This section provides information on the apparatus used for the data collection. It also describes the operating environments and the GFIMU arrangements on the basis of which analysis will be performed.

The field tests were carried out in Calgary, Alberta in different operating environments, including open and urban environments. An open environment is considered to be the one with clear view of sky. The open area data was collected on the University of Calgary campus in the parking lot in front of the Calgary Centre for Innovative Technology (CCIT) building. An urban environment is one where high-rise buildings block GPS signals and create high multipath conditions. This data was collected in downtown Calgary. A number of tests were done in both environments, of which three tests are discussed here, including two in an open environment and one in the urban environment.

5.1.1 Sensors and Equipments

Five MEMS-based Crista IMUs from Cloud Cap Technology Inc. were used to form a GFIMU (as shown previously in Figure 3.2). Each IMU is small in size (5.21 cm x 3.81 cm x 2.54 cm) and weighs only 36.8 grams (Crista IMU ICD 2009). It has a built-in GPS pulse per second (PPS) interface which facilitates the accurate time synchronization of IMU and GPS data. The IMU data was collected at 100 Hz. The other primary piece of equipment used for this research was the NovAtel Synchronous Position, Attitude and Navigation (SPAN™) system. The SPAN™ system consists of a tactical grade Honeywell HG1700 IMU which provides low noise angular and acceleration data at 100 Hz; the system was used for generating a reference solution for error analysis. The inertial data was time tagged internally by the NovAtel SPAN™ OEM4 GPS receiver. The solution was computed in post-mission by integrating the inertial data with GPS using a tightly coupled integration strategy. The software used for this purpose was the GPS/INS Integration Navigation Software (GIINS) (Godha 2006). The reference solution obtained in this way was continuously available, even through periods when satellite signals were blocked. The GPS reference or base station (for differential GPS) was equipped with a dual frequency NovAtel OEM4 receiver connected to a high performance NovAtel 702 antenna, and was set up on the roof top of the CCIT building. At the remote station, a NovAtel 702 antenna was connected with a NovAtel OEMV or OEM4 receiver (different for different tests). An aluminum backpack system with several compartments was used to safely carry the receiver and other testing equipments. Data was logged using different methods in different tests. Tests 1 and 2 described below

were collected using the Position Location and Navigation (PLAN) Group's NavBox which collected data from all five MEMS IMU and remote GPS receiver on a memory card. The remote GPS receiver in these tests was an OEMV receiver integrated in the NavBox. Test 3 described below was collected using a laptop via the use of an edgeport. An edgeport is a device that converts a USB to serial converters for COM port expansion. The remote GPS receiver in this case was an OEM4 receiver.

5.1.2 Test Description

Data was collected with the GFIMU placed on different parts of the body, namely on the back, hands and a foot. This was done so as to compare and quantify the benefits obtained with different rotational dynamics. Moreover, when the GFIMU was attached to the foot, Zero-velocity updates (ZUPTs) were used to keep the velocity errors in bounds. Data collection for each test began with a static initialization period of about 5-7 minutes followed by approximately 30 minutes of walking. Static data was collected at the beginning to facilitate the initial alignment of the IMUs. Figure 5.1 shows the test set-up used in this work for all three placements of the GFIMU.
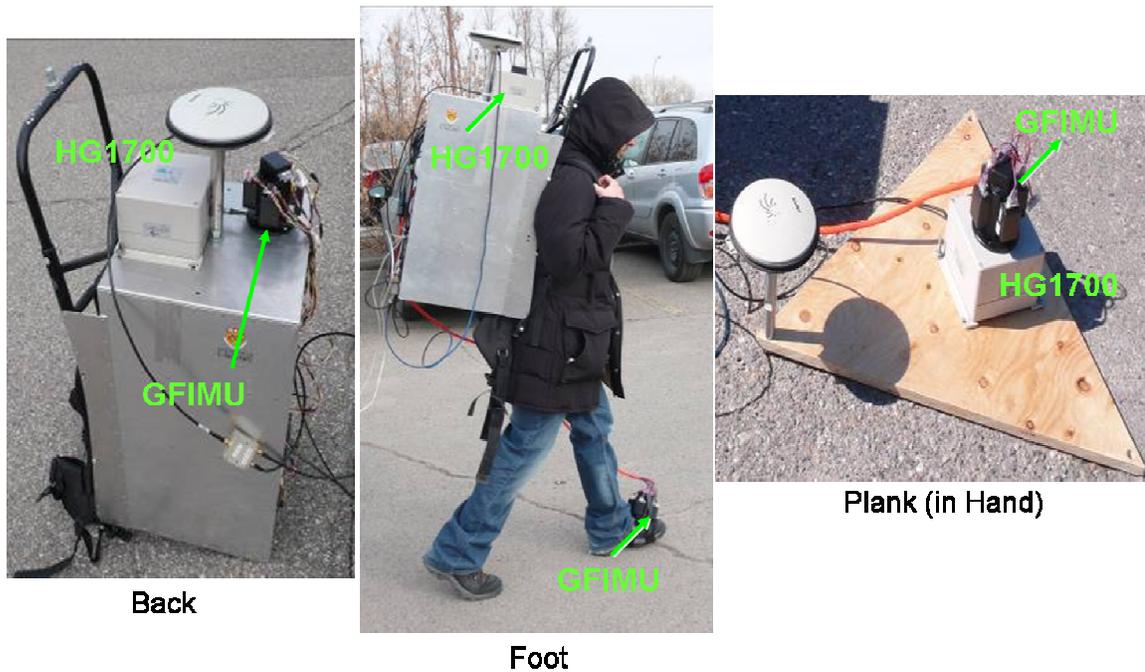
Figure 5.1: Test set-up

For the back case, the GFIMU was attached to the rigid backpack along with the tactical grade HG1700 IMU. The antenna was attached as shown in the figure to reduce the lever arm distance between the antenna and the IMUs.

It should be noted that, when the GFIMU was attached to the foot, the HG1700 IMU was still connected at the top of the backpack system. The prototype GFIMU was rigidly attached to the foot using a thin metal plate. Section 5.3.3 further describes the attachment.

For the hand case, the tactical grade IMU and the GFIMU were attached to a triangular wooden plank along with the antenna. The other equipment including the receivers and cables along with the laptop were kept in the backpack system. The triangular plank was given rotations about all axes (*X*, *Y* and *Z* of GFIMU (Figure 3.3)) for data collection.

5.2 Analysis Procedure

The data reduction and analysis were performed in the following manner. The reference/true solution was obtained by tightly integrating the NovAtel OEM4 GPS receiver with the HG1700 based INS in the SPAN system. Double differencing was used in order to minimize the effect of the atmospheric errors. The baseline was small (< 1 km for the Open Area Test and about 4.4 km for the Urban Area Test), thus the residual, baseline-dependent errors, after GPS differential corrections were small. Processing was done using the original and de-noised measurements. The de-noising methods discussed in Chapter 4 were applied to the accelerometer measurements. The results for both the original and de-noised measurements are discussed for both the measurement and position domains. Measurement domain results include:

      a. GFIMU results, i.e. the specific force and the angular estimates (angular acceleration and square of the angular velocities) obtained from the accelerometer measurements. These are prior to using the EKF discussed in Section 3.6.

      b. GFIN+ estimates of angular velocity and specific force estimates. These are estimated using the GFIN+ EKF.

The position domain results are primarily discussed in terms of the position errors computed using the reference solution obtained as discussed previously. The error results are mostly discussed as horizontal (i.e. 2D) RMS errors or maximum horizontal errors

depending on whichever is appropriate. The percentage probability level for horizontal RMS error is 63-68 % (e.g. Van Digglen 1998).

For the open area test, position accuracy was tested by integrating the GFIN+ with GPS with tight integration software. Since the satellite availability was good, GPS outages were simulated in the trajectory in different regions, i.e. during the rotations and in the linear parts. This allowed analysis of the proposed work and accuracy of stand-alone GFIN+ in different kinds of dynamics.

Having quantified the performance of the designed integrated system under benign operational conditions, the urban area test was then analyzed, which is focussed on performance analysis in more realistic operational conditions. Verification in the urban area is important as compared to the simulated outages, because the satellite availability and geometry plays an important role in the accuracy of the final solution. In urban areas, the conditions were harsh, for example, occurrences of multipath and frequent change in the number and location of satellites, therefore it was important to verify the integration algorithm in these conditions.

5.3 Results

As mentioned earlier, several field tests were conducted in both urban and open areas by placing the GFIMU block on different parts of the body. The results of three tests are discussed here, including for the cases when the:

1. GFIMU was kept on the back in an open area scenario

2. GFIMU was kept in hands in an open area scenario

3. GFIMU was kept on the foot in urban area environment

The analysis is based on the strategies discussed in Section 5.2, which includes analysis on both the original and de-noised measurements.

5.3.1 GFIMU on the Back – Open Area

In separate tests, two users wore the backpack system as shown in Figure 5.1, and walked various routes in the parking lot in front of the CCIT building. GPS data for this test was collected at 2 Hz at the rover and the base receivers. A part of the trajectory is shown here for analysis which involved the user making multiple traverses of the parking lot with hair-pin or zigzag turns. During this test at least seven satellites were visible. The horizontal 2D-RMS of the reference solution was 0.2 m. Figure 5.2 shows the reference trajectory obtained by the SPAN system.
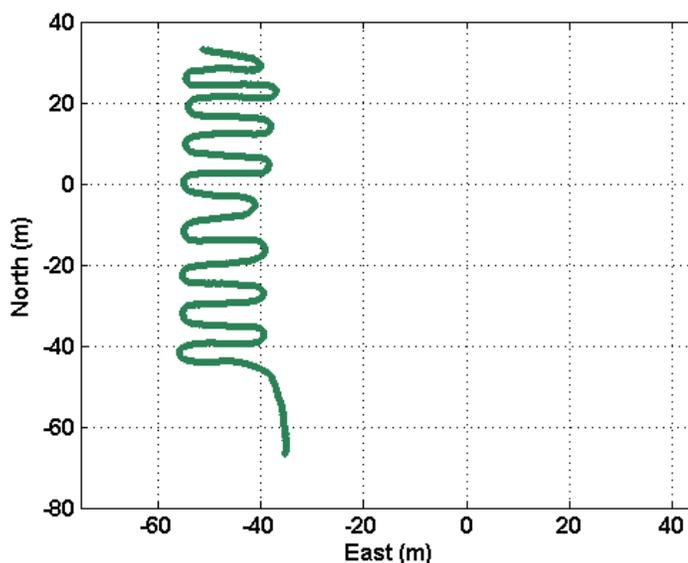

Figure 5.2: Reference Trajectory (Test 1: GFIMU is kept on the back)

It should be noted that the scale on the trajectory plots in this work corresponds to the base station co-ordinates, i.e. (0, 0) in the plot above corresponds to the base station.

The angular velocity measured by the reference HG1700 IMU in this trajectory is shown in Figure 5.3 (only 70 second section in the *X*, *Y* and *Z* axes is shown for visibility). The effect of the aforementioned zigzag turns is clearly visible in the *Z* axis gyroscope output. Since the GFIMU and HG1700 are on the back, the rotations will be highest in the yaw-rate measured by the *Z*-axis gyroscope. The double-peaks every 15 seconds are at about 90 degree/s, corresponding to the two portions of the turn. The measurements of the *X* and *Y*-axis gyroscopes are very small and seem to be noise-like in the same scale of -100 to 100 degrees/s of angular velocity. When examined closely they exhibit a structure corresponding to the subject's gait as shown in Figure 5.4. The *X* axis measurements show a pattern of the movement of the user's shoulders while carrying the backpack system. The *Y* axis output, however, is random and a larger value is seen whenever the user bends on the left or right side.
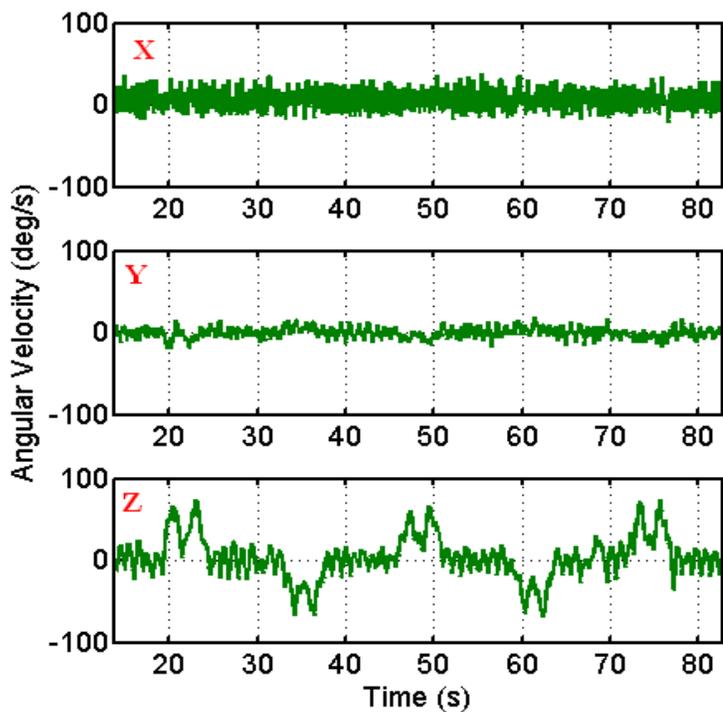
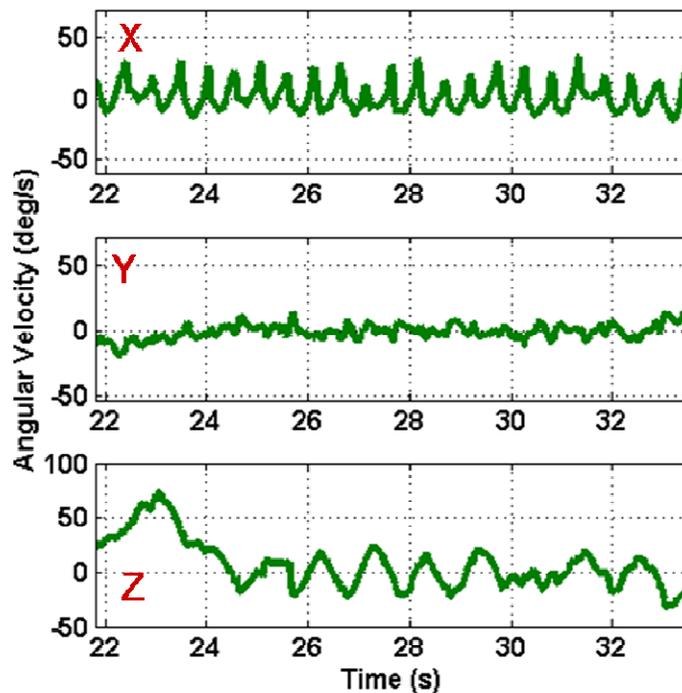**Figure 5.3: Angular Velocity experienced by the HG1700 (Reference IMU)**

Figure 5.4: Close-up of the angular velocity experienced by HG1700

Sections 5.3.1.1 and 5.3.1.2 discuss the GFIMU and GFIN+ results, respectively. This is followed by de-noising results in Section 5.3.1.3.

5.3.1.1 GFIMU Results

The GFIMU results were obtained without using the GFIN+ EKF, i.e. directly from the accelerometer measurements. The angular acceleration was obtained as explained in Section 3.4 and is shown in Figure 5.5 for the Z-component. The angular acceleration for the reference was computed by numerically differentiating the Z-component angular velocity obtained from the HG1700 IMU.
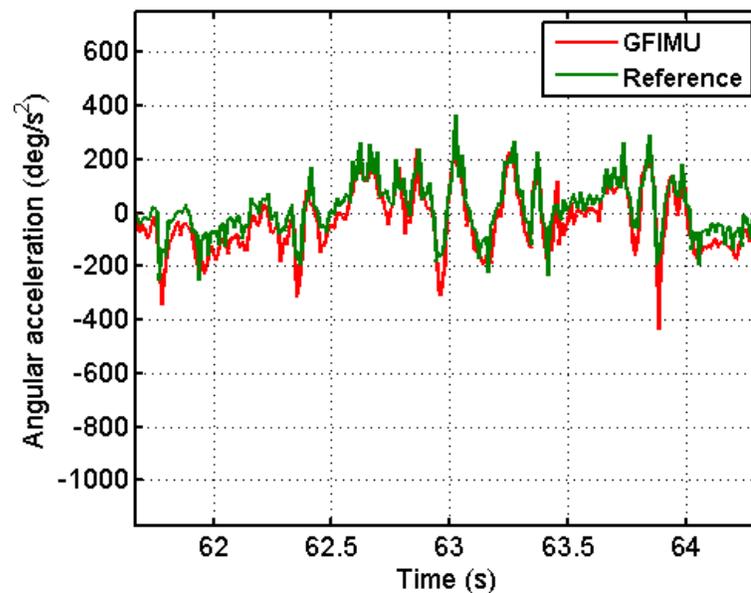

Figure 5.5: GFIMU estimate of the angular acceleration about the body Z-axis

The angular acceleration estimate of the GFIMU follows the reference well, with a slight bias. This bias is mainly due to the biases in accelerometer measurements left after the

calibration (Section 3.3). These accelerometer biases are also magnified because of the pre-multiplication factor $\mathbf{N}_\alpha$ (Equation (3.16)). The two measures of the error amplification discussed in Section 3.4, namely the spectral norm of $\mathbf{N}_\alpha$, $\|\mathbf{N}_\alpha\|_2$, and the product, $\mathbf{N}_\alpha \mathbf{N}_\alpha^T$ are

$$\|\mathbf{N}_\alpha\|_2 = 14.6 \text{ and } \mathbf{N}_\alpha \mathbf{N}_\alpha^T = \begin{bmatrix} 213.5 & -2.6 & 0.4 \\ -2.6 & 214.7 & 1.6 \\ 0.4 & 1.6 & 135.4 \end{bmatrix} \tag{5.1}$$

respectively.

The value of the spectral norm indicates that the bias in the $\mathbf{\alpha}$ estimate of the GFIMU could be more than 14 times that of accelerometer biases, assuming all biases are equal. The matrix product $\mathbf{N}_\alpha \mathbf{N}_\alpha^T$ is proportional to the covariance matrix of the errors in angular acceleration estimate of GFIMU. According to Equation (5.1), the Z-component of the angular acceleration will have less noise compared to the other two components, but overall the noise will be considerably larger than that of the accelerometer measurements.

The square of the angular velocity estimate, $\mathbf{sq}(\mathbf{\omega})$, is shown in Figure 5.6 for the Z-axis for both the GFIMU estimate and the reference. The estimate appears to be heavily biased and very noisy. Inspection of the vertical scale of the plot shows one of the causes of the problem. The square of the angular velocity is mostly close to zero and an exception occurs only when a turn is executed. Thus, because of the small value of the angular velocity, it is masked by the large noise and biases. The cause of the noisy biased

estimate, again, can be seen through the spectral norm and the matrix product. The norm $\left\|\mathbf{N}_{\mathbf{sq(\omega)}}\right\|_2$ is 22.2 and larger than $\left\|\mathbf{N}_{\boldsymbol{\alpha}}\right\|_2$, indicating that biases on the accelerometer measurements may affect the estimate of $\mathbf{sq(\omega)}$ more than that of $\boldsymbol{\alpha}$. The matrix product is given by

$$\mathbf{N}_{\mathbf{sq(\omega)}}\mathbf{N}_{\mathbf{sq(\omega)}}^{T} = \begin{bmatrix} 281.9 & 11.2 & -149.1 \\ 11.2 & 281.5 & -143.7 \\ -149.1 & -143.7 & 281.7 \end{bmatrix}. \tag{5.2}$$

Equation (5.2) indicates that the noise magnification in $\mathbf{sq(\omega)}$ estimate is considerably larger than that of the $\boldsymbol{\alpha}$ estimate and is evenly distributed over the three components. Since the true values of $\mathbf{sq(\omega)}$ are small, the large noise and bias makes the estimate of the square of the angular velocity, which should be a strictly non-negative quantity, negative as can be seen in Figure 5.6. The estimate would have been better if the angular velocity was larger and the accelerometer biases were smaller or mostly accounted for. This will be shown in higher dynamics cases, like when the GFIMU is placed in the hand or on the foot, to be discussed in the following sections.
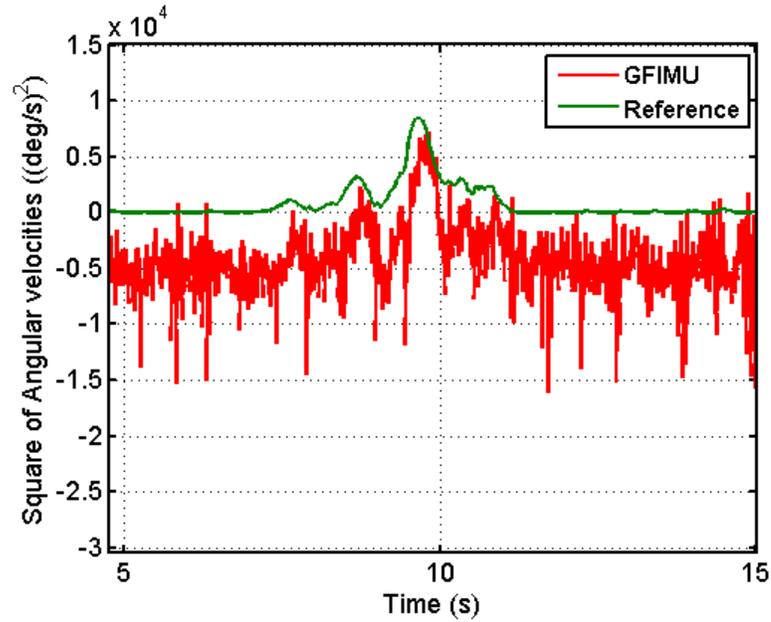
Figure 5.6: GFIMU estimate of the square of angular velocity about the body Z-axis

The specific force estimate of the *Z*-axis from the GFIMU is shown in Figure 5.7. The estimate matches that of the reference. The spectral norm of $\mathbf{N_f}$ is 0.45, indicating that the bias in the specific force estimate of the GFIMU will be less than that of the accelerometer measurements. The covariance matrix of the error in the estimate of $\mathbf{f_O}$ will be proportional to

$$\mathbf{N_f}\mathbf{N_f}^T = \begin{bmatrix} 2.0\times10^{-1} & 6.7\times10^{-4} & -6.1\times10^{-4} \\ 6.7\times10^{-4} & 2.0\times10^{-1} & -4.4\times10^{-3} \\ -6.1\times10^{-4} & -4.4\times10^{-3} & 2.0\times10^{-1} \end{bmatrix} \tag{5.3}$$

with the constant of proportionality being the variance of the accelerometer measurement noise, assuming the variance is equal for all accelerometers. Ideally, the error variance of the specific force estimate would be $1/5^{th}$ of that affecting each of the accelerometer measurements. This is because of the choice of the origin of the body frame as mentioned

in Section 3.2. Suppose, for example, that the origin is taken to coincide with the uppermost tri-axial accelerometer rather than four times closer to the center of the coplanar accelerometers' plane. In this case, the specific force estimate of the GFIMU will be completely determined by the top accelerometers. $\|\mathbf{N_f}\|_2$ would be equal to 1, as would be the diagonal elements of $\mathbf{N_f}\mathbf{N_f}^T$. Thus, the choice of the origin of the GFIMU frame is optimal in the sense that it minimizes $\|\mathbf{N_f}\|_2$.
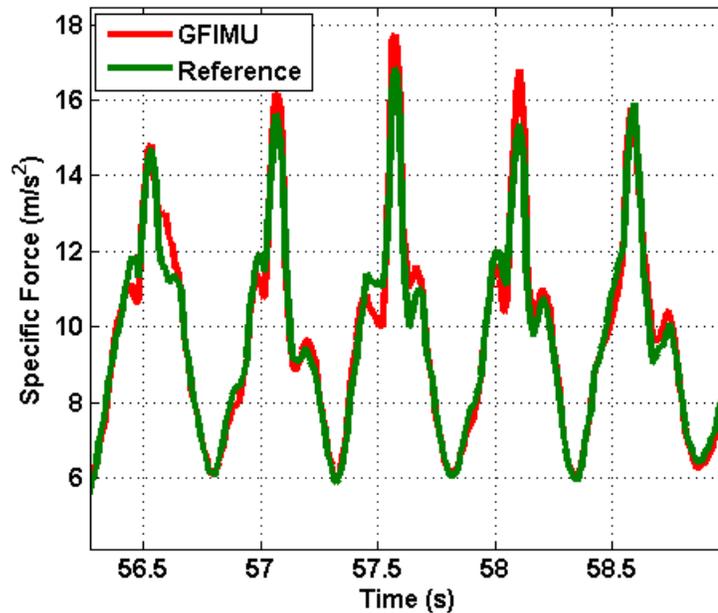

Figure 5.7: GFIMU estimate of the specific force along the body Z-axis

5.3.1.2 GFIN+ Results

The GFIN+ results at the angular velocity level are shown first, followed by the position level results.

- Angular Velocity Results

GFIN+ angular velocity estimates can be compared with that of SIN by estimating the errors in both with respect to the reference HG1700 IMU. Figure 5.8 shows the errors in the angular velocity estimate of GFIN+ and SIN.
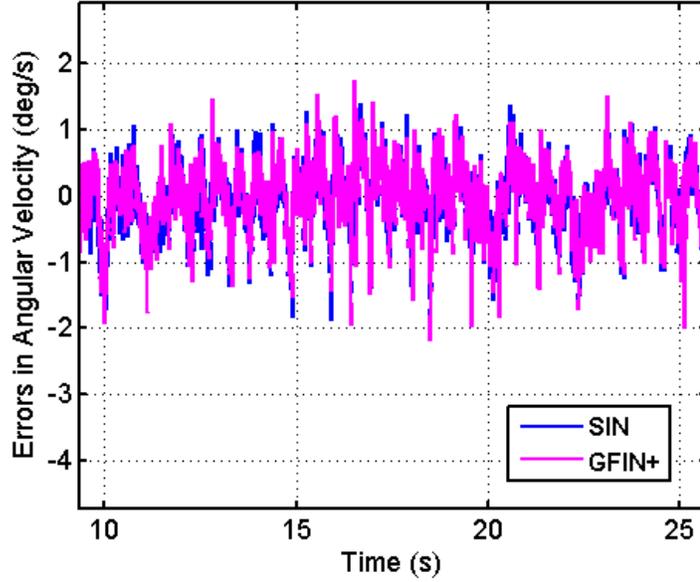

Figure 5.8: Errors in the Z-component of angular velocity estimates from SIN and GFIN+ EKF

The differences between the GFIN+ estimates and SIN gyroscope measurements are very subtle. This can be explained by reference to measurement noise covariance matrix $\mathbf{R}$ given by Equation (3.38). $\mathbf{R}$ depends on the gyroscope noise covariance matrix $\mathbf{Q_g}$ and the covariance of the error in $\mathbf{N_{qu(\omega)}}\tilde{\mathbf{F}}_k$, which is $\mathbf{N_{qu(\omega)}Q_a N_{qu(\omega)}^T}$. The noise parameters of the accelerometers and gyroscopes were determined by prior testing (Section 2.2.3.1, Table 2.1) of the MEMS IMUs and the covariance matrices were set at:

$$\mathbf{Q_a} = 5\times10^{-5}\mathbf{I}_{15}\left(m/s^2\right)^2 \tag{5.4}$$

$$\mathbf{Q_g} = 6\times10^{-6}\mathbf{I}_3\left(rad/s\right)^2. \tag{5.5}$$

The average of the diagonal elements of $\mathbf{N}_{\mathbf{qu}(\omega)}\mathbf{N}^T_{\mathbf{qu}(\omega)}$ matrix is 235. This indicates that the error variance of the estimates of $\mathbf{qu}(\omega)$ is (2.35×10^2).(5×10^{-5}), that is of the order of 10^{-2}. Thus, $\mathbf{Q}_g$ is four orders of magnitude smaller, which means that the gyroscope measurements will dominate the filter's estimate of ω. The impact of the accelerometers on the angular velocity estimates could be increased by employing the noise reduction techniques described in Chapter 4. Using accelerometers with better noise specifications, or using a lower quality gyroscope or a larger spacing between accelerometers could also lead to more effective accelerometer measurements, as compared to gyroscopes.

- Position Results

The average number of satellites was nine during the part of the trajectory shown in Figure 5.2, therefore SIN and GFIN+ plots mostly overlap with the reference. To quantify the performance of GFIN+ and SIN, two GPS outages of 10 s each were simulated. The first outage is during a relatively straight part of the trajectory, (i.e. north value of ~ -10 m), and the second outage is during a turn (i.e. north value of ~ -35 m). In both outages, GFIN+ yields smaller horizontal errors. Figure 5.9 shows the trajectory plot with the two outages.
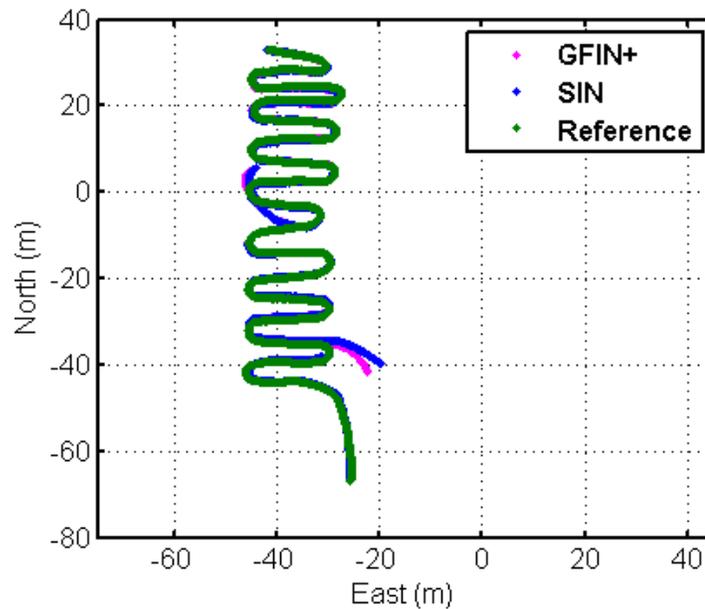
Figure 5.9: SIN and GFIN+ Tight Integration Position Solutions with two 10 s simulated GPS outages

The maximum horizontal error at the end of the first outage for GFIN+ is 16.7 m and for SIN is 17.6 m. For the second outage, a greater improvement of about 21.5 % is seen, with maximum horizontal errors for GFIN+ of 8.4 m and for SIN of 10.7 m. The second outage is simulated during a turn, supporting the theoretical development of Chapter 3 and suggesting that more improvement in the angular velocity estimate can be achieved when angular dynamics are high.

Even when the angular velocity estimate from GFIN+ is very similar to that from the aiding gyroscope, GFIN+ generally has better performance because the specific force estimate of GFIN+ would be better than SIN.

The horizontal RMS errors in SIN and GFIN+ during the outage simulation are summarized in Table 5.1.

5.3.1.3 Results after De-noising

This section discusses the results after the accelerometer measurements are de-noised using the de-noising techniques discussed in Chapter 4. Wavelet de-noising results are discussed first, followed by LPF de-noising results.

- Wavelet De-noising Results

Wavelet de-noising, discussed in Section 4.5, was implemented to de-noise the accelerometer signals. These de-noised accelerometer measurements were used to get de-noised GFIMU measurements. The de-noised GFIMU measurements were input into the GFIN+ EKF to get the de-noised GFIN+ measurements. The de-noised GFIN+ specific force and angular velocity estimates were used as a virtual IMU to integrate with GPS in the GPS/INS tight integration software.

The tight integration position solutions for SIN, GFIN+ and de-noised GFIN+ are shown in Figure 5.10. As can be seen, the solutions overlap each other. The RMS difference with respect to the reference is around 0.5 m. This is because GPS was dominant during this part of the trajectory. To analyse the performance of the de-noised GFIN+ and compare it with the GFIN+ and SIN solutions, the same outages of 10 s as described earlier were simulated (Figure 5.9).
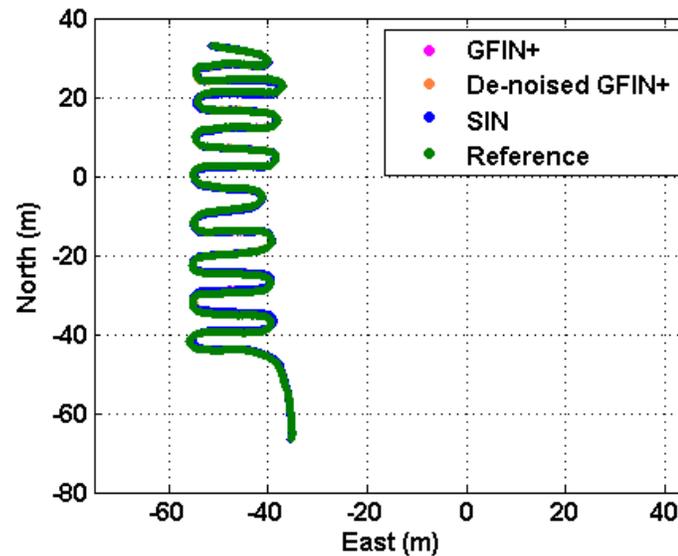
Figure 5.10: Position solutions for SIN, GFIN+ and De-noised GFIN+

Figure 5.11 shows the trajectory of all three solutions, namely SIN, GFIN+ and de-noised

GFIN+, with the outages simulated. For the first outage, which is in the linear region, the

maximum horizontal error for the de-noised GFIN+ output is 10.1 m. This is less than

both SIN and GFIN+ maximum horizontal errors, which are 17.6 and 16.7 m,

respectively. However, for the second outage the de-noised GFIN+ gives a maximum

horizontal error of 14.1 m, which is larger than that of the SIN (10.7 m) and GFIN+ (8.4

m) solution. This increase in the de-noised GFIN+ outputs during the second outage may

be because of the turn and its associated higher dynamics. Thus, it is possible that the de-

noising engine (wavelet de-noising, in this case) is removing the actual motion during the

larger dynamics case, due to a sudden increase in frequency, treating it as high frequency

noise. This is likely because of the sudden increase in heading error at the beginning of

the outage, which causes a deviation from the true trajectory. This degradation in heading

from the start of the outage causes the error to further increase. Thus, the performance

comes out to be worse than SIN or GFIN+. Figure 5.12 shows angular velocity of de-noised output and the reference measured by the *Z* gyroscope, for a part of the duration where the second outage is simulated. It can be seen the angular velocity of the de-noised output has a deviation of about 1-2 deg/s from that of the reference. Similar errors can be seen for the other axes. This error finally leads to the error in position.

For the linear part of the outage simulation, the dynamics are low and therefore de-noising the measurements leads to an improvement of over 40 %. However, it should be noted that the horizontal RMS error for de-noised GFIN+ is less than that of either SIN or GFIN+. The horizontal RMS errors for all the three outputs are summarized in Table 5.1.
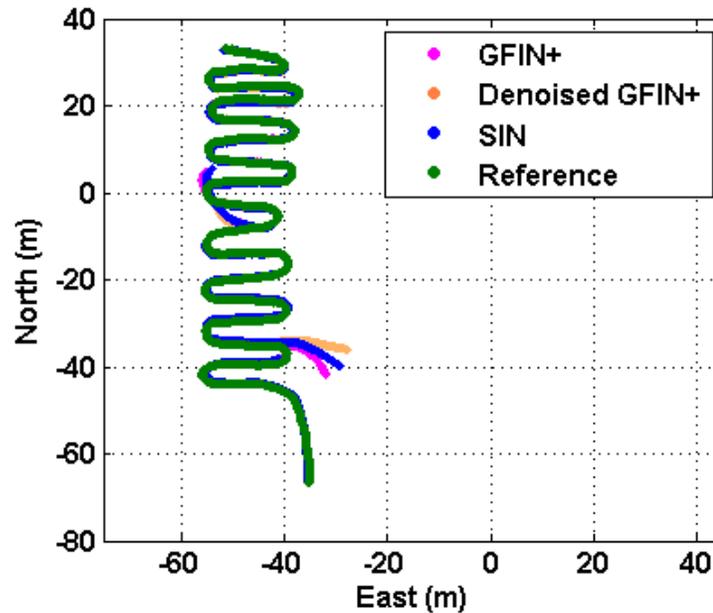

Figure 5.11: SIN, GFIN+ and De-Noised GFIN+ Tight Integration Position Solutions with two 10 s simulated GPS outages
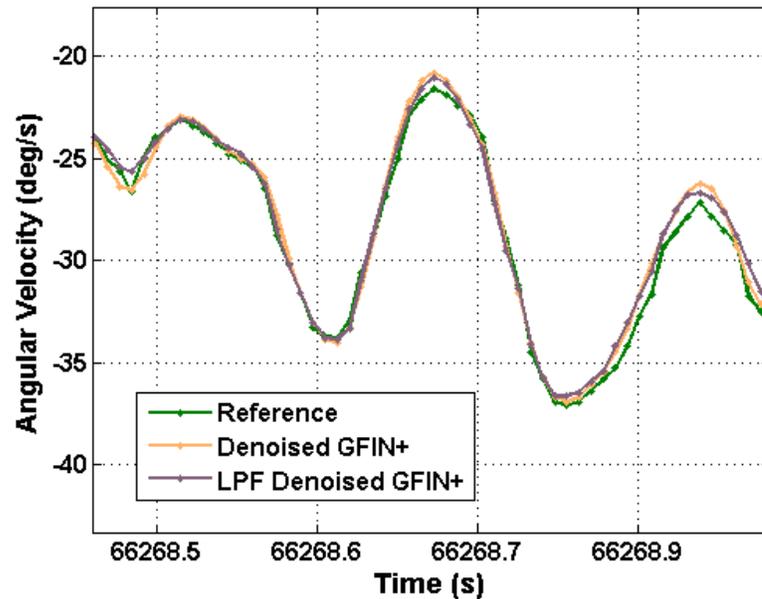
Figure 5.12: Reference, Wavelet and LPF De-Noised GFIN+ Angular Velocity in *Z* axis

Table 5.1: Horizontal RMS errors for GFIMU on the back

	Horizontal RMS error (m)	Improvement with respect to SIN
SIN	1.90	---
GFIN+	1.81	4.7 %
De-noised GFIN+	1.53	19.5 %

- LPF De-noising Results

The Butterworth LPF described in Section 4.6 is used to de-noise the accelerometer measurements. These LPF de-noised accelerometer measurements are then used to determine the LPF de-noised GFIN+ estimates of angular velocity and specific force in the same way as for wavelet de-noised measurements. The maximum horizontal errors for the LPF de-noised position solution come out to be 15.2 m and 15.0 m for the first

and the second outages, respectively. These errors are larger than those of wavelet de-noised errors. Low pass filtering removes the noise above the cut-off frequency; therefore the noise is still present in the region below the cut-off frequency. Since low pass filtering spreads the energy of inertial sensor signals on a high number of coefficients, it is difficult to discriminate signals from a noisy background. This degrades the overall performance. The horizontal RMS error for the LPF de-noised output is 1.80 m.

5.3.2 GFIMU in Hand – Open Area

In this test, the wooden plank was used to mount the antenna, HG1700 IMU and the GFIMU block as shown in Figure 5.1. The data was collected in an open area on the roof of the CCIT building, by rotating the wooden plank about all three axes. First, the data was collected in a static mode, after which two rounds were taken by almost continuously moving the plank in all directions.

 Figure 5.13 shows the reference trajectory derived from the SPAN system. The duration of the trajectory was about eight minutes. The base GPS data for this test was collected at 5 Hz. During this test at least five satellites were visible. The number of satellites was reduced because the antenna was connected to the wooden plank. Since the plank was being continuously rotated, the signals became obstructed because of random rotation of the antenna with the plank. The horizontal estimated RMS accuracy of the reference solution for this test was 0.25 m.
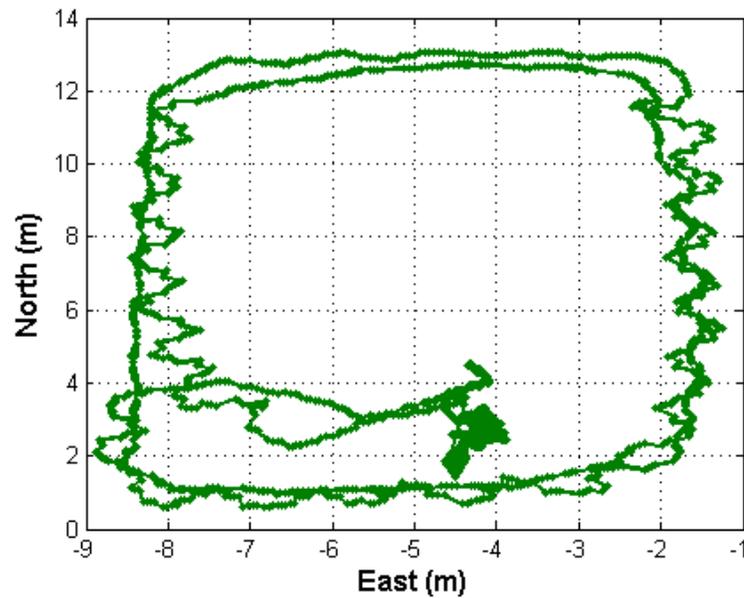
Figure 5.13: Reference Trajectory - GFIMU in hand

Figure 5.14 shows the angular velocity measured by the HG1700 IMU. Until about 550 s, the user was stationary and rotated the plank at a particular place, after which the user took two rounds, while continuously rotating the plank about all axes, which is from about 650 s to 730 s in the figure. This can be seen by the scale of the angular velocity increasing one by one for *X*, *Y* and *Z* axes in the stationary region. The *Y* scale from Figure 5.14 shows that the angular rotation of the IMU ranges from approximately -200 deg/s to +200 deg/s, which is larger than what was experienced when the IMU was kept on the back.
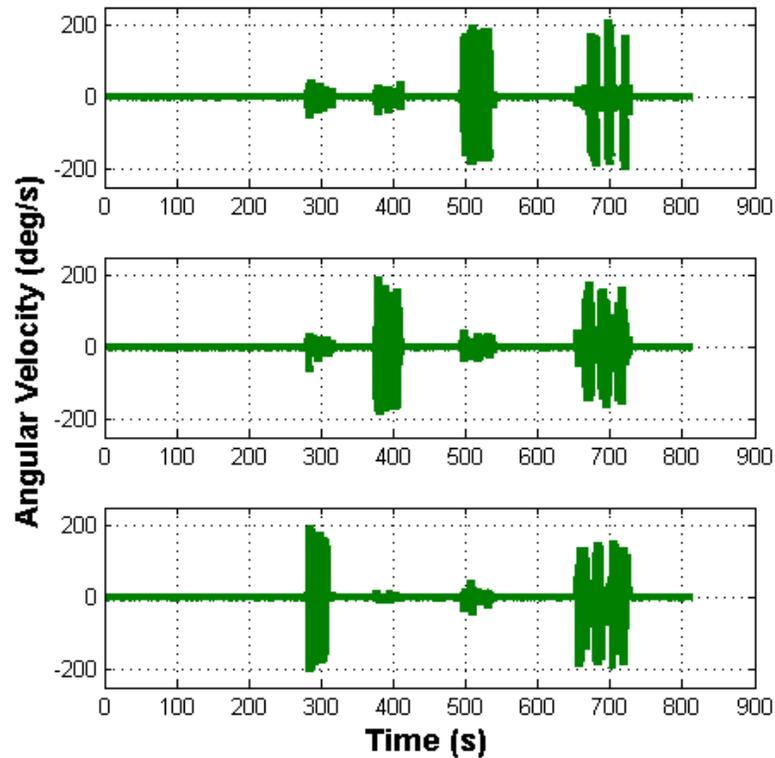
Figure 5.14: Reference Angular Velocity (HG1700 in hand)

5.3.2.1 GFIMU Results

The angular accelerations and the squares of the angular velocity estimate for the Z-axes

of a GFIMU in hand are shown in Figure 5.15 and Figure 5.16. respectively. It can be

seen the rotations are higher when GFIMU is held in the hands as compared to the case

when the GFIMU is kept on the back. Angular acceleration, in the hand case, ranges from

-1500 deg/s^2 to +1500 deg/s^2 whereas in the back case, it is from -400 to 400 deg/s^2

(Figure 5.5). Similarly, the square of the angular velocity is larger when the GFIMU is in

hand. Due to larger rotational dynamics, it can be seen that the estimates of both the

square of the angular velocity and the angular acceleration follow the reference. When

the GFIMU is on the back, the square of the angular velocity is very noisy and highly

biased; however in this case, the square of angular velocity has better accuracy. This is because the rotations are higher and therefore, the noise is not masking the motion. The negative overshoots in square of angular velocity are seen when the angular velocity is near zero. This is because square of angular velocity estimate would be a smaller quantity and thus, it overshoots to become negative because of noise amplification.

Similarly, the specific force estimate of the GFIMU, although not shown here, follows the reference well.
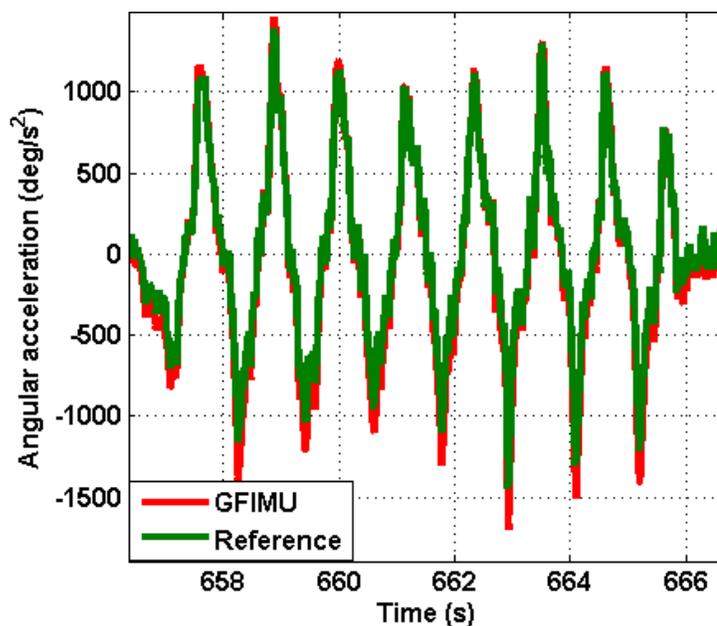

Figure 5.15: *Z* **axis Angular Acceleration estimates for GFIMU in hand**
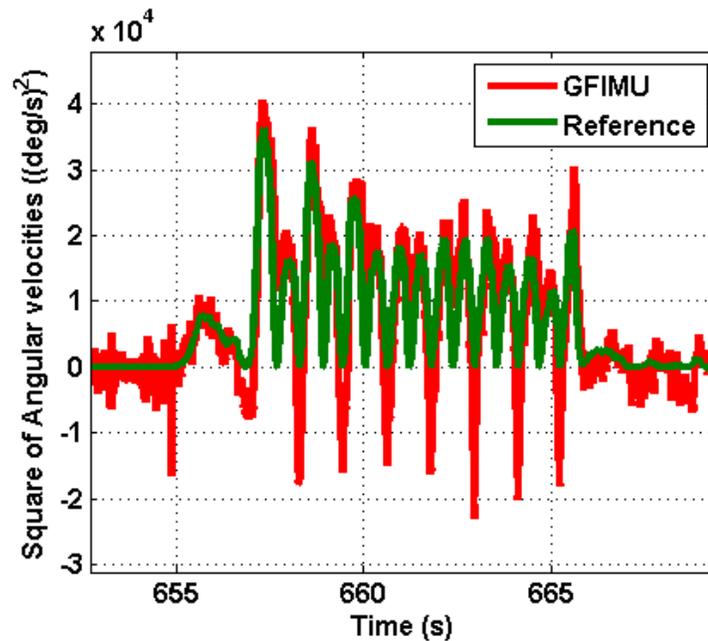
Figure 5.16: Z axis Square of Angular Velocity estimates for GFIMU in hand

5.3.2.2 GFIN+ Results

Similar to Section 5.3.1.2, the GFIN+ results are again discussed in terms of angular velocity errors and position errors.

• Angular Velocity Results

The angular velocity estimates of the GFIN+ are shown in Figure 5.17, along with that of the reference. Only 25 s of the data is shown here. The figure indicates that the GFIN+ estimates follow the reference in all three axes. The trend is similar for the rest of the data.

Figure 5.17: Angular velocity estimates from the GFIN+ EKF in *X*, *Y* and *Z* axes respectively (top to bottom) – In Hand
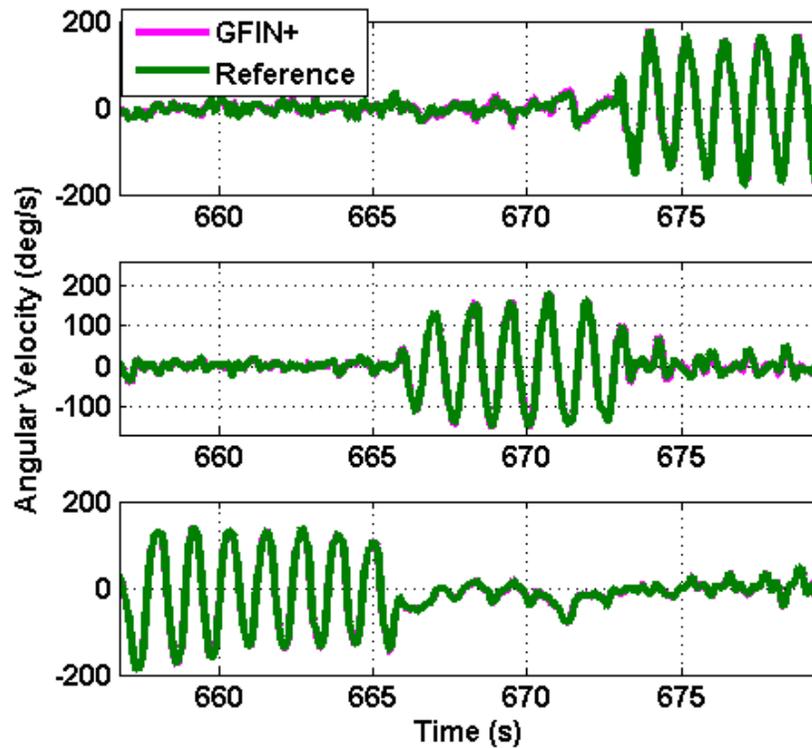
The comparison of the errors in the angular velocity estimates of GFIN+ and SIN with respect to the reference shows a subtle difference, as for the case of the GFIMU on the back (Figure 5.8). The reason for the minor differences between the GFIN+ and SIN errors is the same as before, namely the gyroscope measurements are being trusted more than the accelerometer measurements.

- Position Results

Since it is an open area, the trajectories obtained by processing the GFIN+ and SIN data overlap with the reference position solution. Thus, as discussed before, two outages of 10 s each are simulated. The first outage is simulated in a relatively straight portion of the

trajectory (~ 13 m North and ~ -4 m East). The second outage is simulated during a rotating part of the trajectory (~ 11 m North and ~ -1.5 m East) (Figure 5.13). The maximum horizontal errors at the end of the first outage for GFIN+ and SIN are 76.0 m and 76.1 m, respectively. For the second outage the maximum horizontal errors for GFIN+ and SIN respectively are 63.2 m and 74.0 m. Clearly, in the region with higher dynamics, the GFIN+ shows more improvement (14.6 %) as compared to that in the first outage where the improvement is a mere 0.13 %.

5.3.2.3 Results after De-noising

• Wavelet De-noising Results

The wavelet multi-resolution analysis is used to de-noise the accelerometer signals, in order to determine the de-noised GFIMU estimates of specific force and angular velocity. The errors in the angular velocity and specific force estimates of the wavelet de-noised GFIN+, GFIN+ and SIN systems with respect to the reference are shown in Figure 5.18 and Figure 5.19.
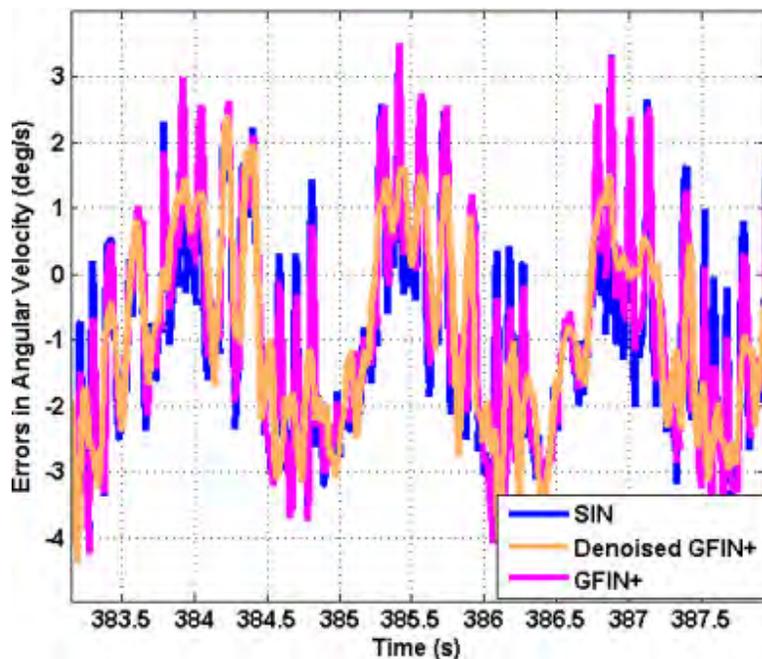
Figure 5.18: *Y* **axis Errors in Angular Velocity for SIN, GFIN+ and Wavelet De-Noised GFIN+**
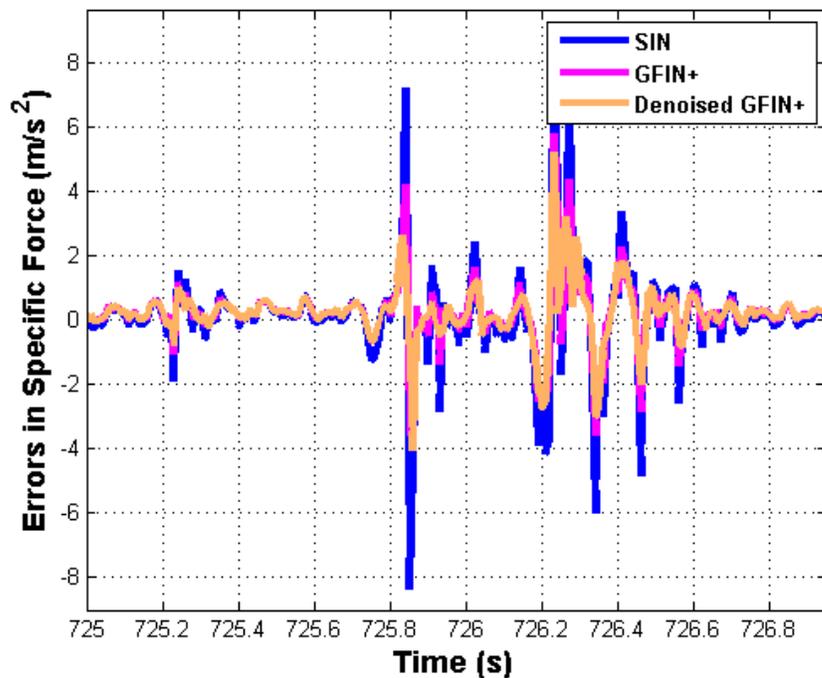

Figure 5.19: *Z* **axis Errors in Specific Force for SIN, GFIN+ and Wavelet De-Noised GFIN+**

As stated earlier, the errors in the angular velocity estimates for GFIN+ are similar to those of SIN. However, errors in the de-noised GFIN+ estimates are less than the corresponding estimates for GFIN+ and SIN. This is because, when the accelerometer measurements are de-noised, the accelerometer noise variance input into the GFIN+ EKF is lower and therefore, the filter appropriately weighs and uses both the accelerometer and gyroscope measurements.

The errors in the estimates of the specific force in de-noised GFIN+ are similar to that of GFIN+; however, the errors for both de-noised GFIN+ and GFIN+ are much lower than those of SIN. This is because the noise is averaged out in GFIN+ specific force measurements, because five tri-axial accelerometers are being used.

For the position domain results, the same two outages are simulated as before. For the first outage, the maximum horizontal error for the wavelet de-noised GFIN+ output is 46.5 m, thus showing an improvement of 39 %. In the second outage, the maximum horizontal error for de-noised GFIN+ is 40.1 m, which is again an improvement of 46 %. Thus, in both cases, wavelet de-noised GFIN+ shows an improvement and has better performance than both the GFIN+ and SIN outputs.

- LPF De-noising Results

For the LPF de-noised measurements, the first outage has the maximum horizontal error of 70.6 m while that of the second outage is 48.8 m. These are larger than those of the

wavelet de-noised outputs. The horizontal RMS errors are summarized in Table 5.2 for all the outputs.

Table 5.2: Horizontal RMS errors for GFIMU in hand

	Horizontal RMS error (m)	Improvement with respect to SIN
SIN	6.02	---
GFIN+	5.88	2.3 %
De-noised GFIN+	3.56	40.9 %
LPF De-noised GFIN+	4.95	17.8 %

5.3.3 GFIMU on Foot – Urban Area

The GFIMU was attached on a foot as shown in Figure 5.20. A custom designed cross metal plate was designed to rigidly fix the GFIMU on the foot. It had four holes drilled into it to allow rigidity of the block relative to the foot. The cross plate was sufficiently thin to be inserted in between the laces as shown in the figure. The GFIMU block was screwed tightly to the plate and finally, repeated rounds of duct tape were used to ensure rigidity and stability during walking.

The results reported here are for testing in Downtown Calgary. The data was collected around a loop consisting of 8th Street SW and 6th Street SW, between 3rd Ave SW and 4th Ave SW. A part of the data is shown here for analysis. The duration of this part of the test was about 14 minutes. The horizontal RMS accuracy of the reference solution was 0.51 m.

Figure 5.20: Steps to attach GFIMU on Foot

Data collection started with an initialization period of about five minutes in the parking lot near 8th Street SW. Figure 5.21 shows the satellite availability plot of the reference trajectory derived by the SPAN system where the number of satellites used by SPAN along the trajectory is displayed. The parking lot near 8th St SW from where the test started had more than four satellites. During the 7th St and 4th Ave part of the trajectory, there were taller buildings leading to signal obstruction and multipath. Therefore, the number of satellites was between zero and four for about 48 % of the trajectory. Along with poor satellite visibility, there was poor satellite geometry, thus creating a very demanding environment for GPS-based navigation. The data rate for the base and remote receivers for this test was set at 20 Hz and some gaps were observed in the data due to improper logging. Therefore, the range data for some epochs was missing, which created additional outages, even in the open area.
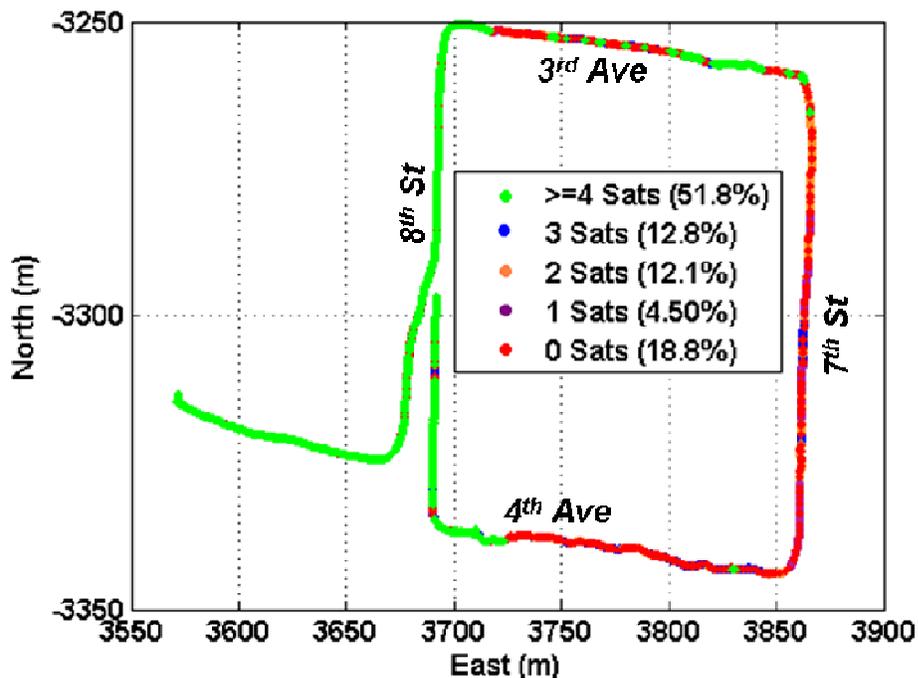
Figure 5.21: Satellite Availability Plot of Reference Trajectory

As mentioned previously, the reference IMU was kept on the back pack system, while the GFIMU block was attached to the foot. Therefore, since the foot experienced different rotational dynamics than the back, the reference IMU had different angular and specific force measurements than the GFIMU. Thus, only position results were analyzed. During post processing, automatic zero velocity updates were used. The automatic ZUPTs detection is built in the GIINS software (Godha 2006).

5.3.3.1 GFIN+ Results

Figure 5.22 shows the trajectory obtained by SIN and GFIN+ outputs. As can be seen, the GFIN+ solution shows slight improvement as compared to the SIN solution. The

horizontal RMS error for SIN is 4.8 m and that for GFIN+ is 4.1 m, thus showing an improvement of 15 %. This improvement in GFIN+ can be attributed to less noisy estimates of the specific force. Section 5.3.3.2 describes the wavelet and LPF de-noised results.
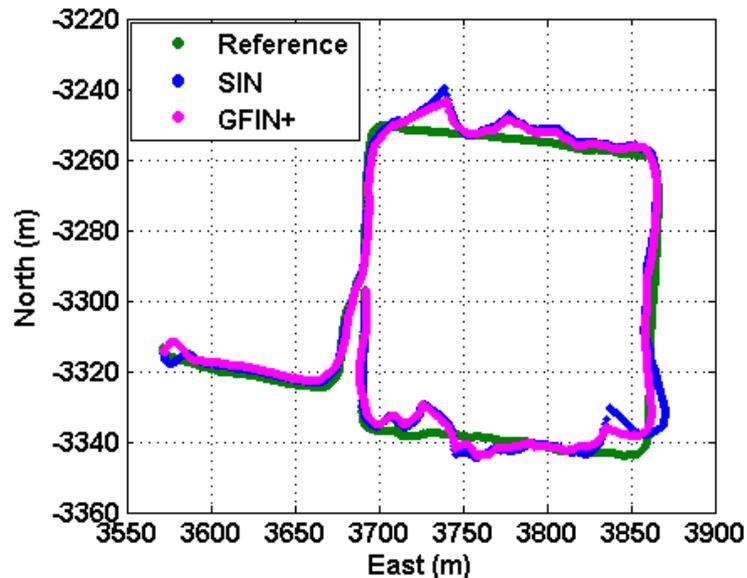
Figure 5.22: SIN and GFIN+ Tight Integration Position Solutions – On Foot

5.3.3.2 Results after De-noising

Figure 5.23 shows the trajectory for the de-noised outputs along with the GFIN+, SIN and reference trajectories. It can be seen that whenever GPS is not available, the wavelet de-noised GFIN+ has better accuracy than the GFIN+ and SIN outputs. For instance, in Figure 5.24, a detailed part of the trajectory is shown. It can be seen that although the SIN output drifts by about 12 m to the north from the nominal value of the reference, the wavelet de-noised GFIN+ has a lower drift of about 5 m in this case.

Figure 5.23: SIN, GFIN+, De-Noised GFIN+ and LPF De-Noised GFIN+ Tight Integration Position Solutions – On Foot
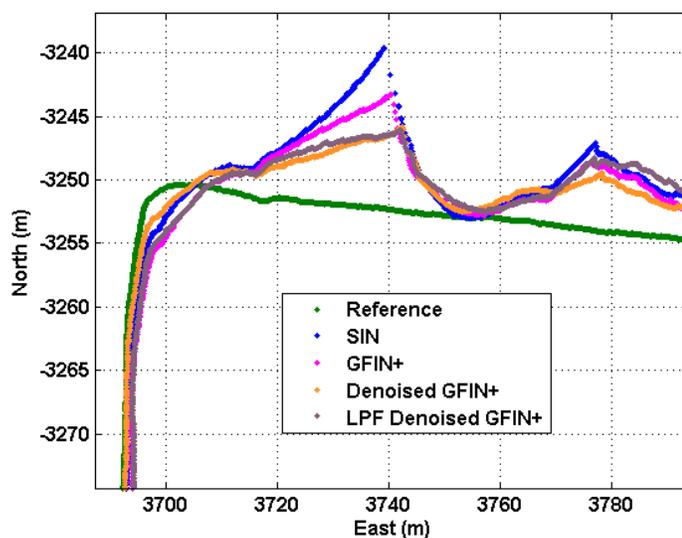
Figure 5.24: Detail of a part of the trajectory

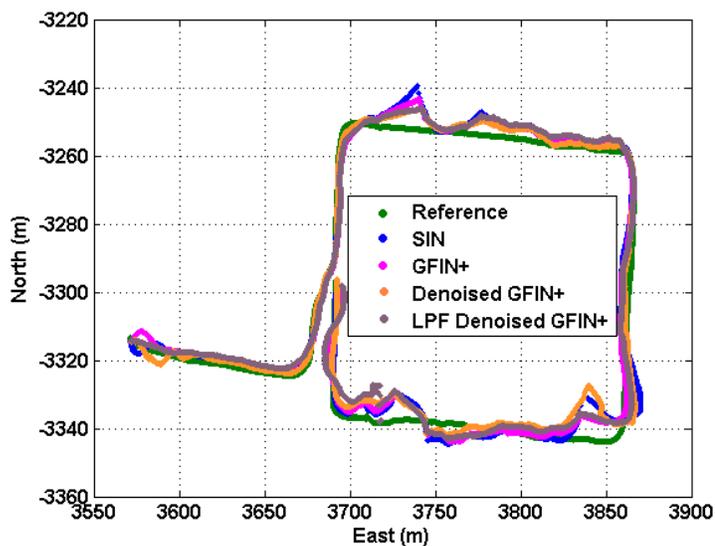A similar observation can be made for the LPF de-noised GFIN+ solution. However, when the LPF de-noised solution is examined for the whole trajectory, it is observed that it loses accuracy at different points, thus degrading its overall accuracy. A part of the

trajectory is shown in Figure 5.25 where the LPF de-noised GFIN+ loses its accuracy. This can be because some measurements might have been removed as noise due to high foot rotation, resulting in the LPF de-noised GFIN+ solution having poorer performance than the other solutions.
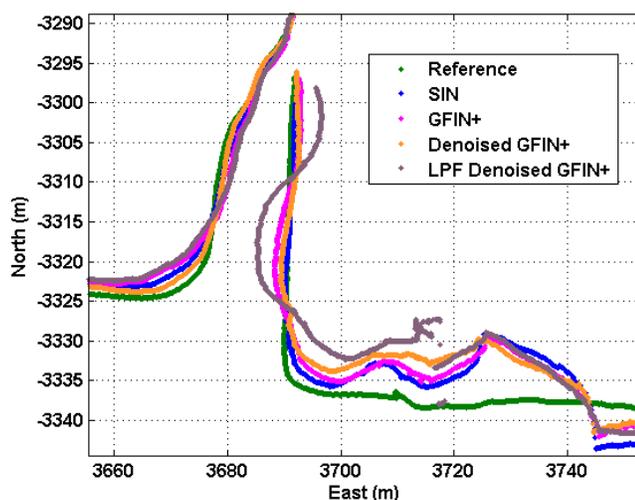
Figure 5.25: Detail of a part of the trajectory: Poor solution for LPF De-noised GFIN+

The horizontal RMS errors are summarized in Table 5.3. The GFIN+ solution shows an improvement of 12 %, whereas the wavelet de-noised GFIN+ solution shows an improvement of 31 %. The LPF de-noised GFIN+ solution has poorer performance as compared to that of SIN, due to the reasons mentioned previously.

Table 5.3: Horizontal RMS errors for GFIMU on foot

	Horizontal RMS error (m)	Improvement with respect to SIN
SIN	4.80	---
GFIN+	4.22	12.1 %
De-noised GFIN+	3.32	30.8 %
LPF De-noised GFIN+	4.93	---

Chapter Six: Conclusions and Recommendations

This chapter discusses conclusions and recommendations for further research.

The major contribution of this research was to evaluate and assess the performance of a gyroscope-aided accelerometer configuration integrated with a GPS receiver for pedestrian navigation. The primary pieces of equipments used for this work were MEMS-based Crista IMUs (from Cloud Cap Technology Inc.) and NovAtel OEM4/OEMV receivers. The NovAtel SPAN system consisting of a tactical grade IMU HG1700 integrated with GPS was used as a reference.

The main motivation behind using an accelerometer configuration to determine the angular velocity of a body was because gyroscopes remain expensive. Also, since accelerometers are smaller in size, have lower cost and are more developed, using an accelerometer configuration is beneficial, particularly for pedestrian navigation. Moreover, a low quality, low cost gyroscope along with an accelerometer configuration is better than just a low cost gyroscope. Therefore, an accelerometer configuration was used to determine both the specific force and angular velocity. These were then integrated with GPS as a virtual IMU measurement.

For this work, a novel accelerometer configuration was used. The configuration consisted of five MEMS tri-axial accelerometers rigidly attached to a custom designed block. It allowed repeatable and rigid fixation. The configuration was used to determine the dynamics of the body, and allowed exploring redundancy benefits, as only four tri-axial accelerometers are required for a feasible accelerometer configuration. The calibration

technique used, allowed determination of initial estimates of biases and misalignment error in all the accelerometers.

The data was collected in different environments such as open and urban areas, by placing the IMUs on different parts of the body. The different placements experienced different dynamics and allowed a performance analysis for various cases. The specific placements were the GFIMU on the back, in hands and on a foot.

The performance of the integrated GPS/GFIN+ system was evaluated both at the angular velocity level and the position level. Position results were evaluated on the basis of horizontal RMS position errors or/and maximum horizontal errors with respect to the reference solution. The results were compared to those based on a single IMU based INS integrated with GPS. Wavelet and low pass filter de-noising techniques were applied on the sensor signals, and de-noised GFIN+ performance was evaluated in a similar manner. Outages were simulated in open environments to evaluate performance in the absence of GPS.

6.1 Conclusions

The major conclusions are as follows:

1) It was shown that, when the GFIMU was kept on the back, the overall angular velocity experienced by the system was very small. However, since the trajectory was chosen to contain zigzags, the maximum angular velocity experienced along the Z axis was 90 deg/s during turns. This was not the case when the GFIMU was in a hand (up to 200 deg/s) or on a foot (400 – 500 deg/s). Due to additional

rotations, the angular velocities experienced were larger and hence, performance analysis for various cases of rotational dynamics was done.

2) The GFIMU estimate of the angular acceleration followed the reference with a slight bias but the square of the angular velocity was highly biased and noisy when the GFIMU was on the back. When the GFIMU was in the hand, both the angular acceleration and square of the angular velocity followed that of the reference. This was because the rotation was higher and therefore, the noise did not mask the motion. GFIMU results for the foot case were not discussed as the reference IMU was kept on the back and therefore experienced different rotations.

3) It was observed that the angular velocity errors from the SIN and GFIN+ systems were similar, because the gyroscope measurements were being weighted higher than the accelerometer angular estimates. Therefore, the accelerometer measurements were de-noised, and the accelerometer-derived angular estimates were also used in the final estimation of angular velocity.

4) For the position domain results, the following results were obtained:

   a. For the case of the GFIMU system on the back in open areas, two GPS outages of 10 s each were simulated. The GFIN+ showed an improvement of 5 % and 22 % in the maximum horizontal errors. In the de-noised outputs, the wavelet de-noised GFIN+ showed an improvement of 43 % as compared to SIN for the first outage. However, for the second outage, due to sudden increase in dynamics, the de-noised GFIN+ showed slightly more errors than GFIN+ and SIN. This increase in dynamics can be

attributed to the removal of high frequency noise and therefore, of high dynamic motion. Similar observations were seen for LPF de-noised GFIN+. However, the horizontal RMS error for wavelet de-noised GFIN+ was less than that of both SIN and GFIN+, showing an improvement of 20 % with respect to SIN.

b. For the case of the GFIMU in the hand in open areas, GFIN+ showed no significant improvement for the first outage, but showed an improvement of 15 % for the second outage. De-noising results were more promising for this case. Improvements were seen for both the angular velocity and specific force estimates of the GFIN+ after de-noising. Wavelet de-noised GFIN+ showed an improvement of 39 % for the first outage while an improvement of 46 % was seen with respect to SIN for the second outage. The LPF de-noised results were not as good as wavelet de-noised results but better than both GFIN+ and SIN. The wavelet de-noised GFIN+ showed an improvement of 41 % in horizontal RMS error, better than both GFIN+ and LPF de-noised GFIN+.

c. For the case of the GFIMU on foot, the data analysed was collected in downtown Calgary. Since there were many instances of natural outages and multipath situations, no outages were simulated for analysis. The horizontal RMS errors were used as a measure to determine the performance of the system. The GFIN+ and wavelet de-noised GFIN+

showed improvements of 12 % and 31 %, respectively. However, the results for the LPF de-noised solution did not show improvement.

5) The ultimate conclusion of this research is that the GPS/GFIN+ integrated solution is a better option than a single IMU-based INS integrated with GPS, given the accelerometer and gyroscope performance specifications considered herein. Moreover, wavelet de-noising improves the results by an average of 30 % in most of the cases considered. Low pass filtering improves results in some cases, but not in a reliable and consistent manner, unless more testing and analysis is done to confirm the results obtained in this work.

6) The results were determined using Crista MEMS IMUs from Cloud Cap Technology which were five years old. Therefore, it is noted that with the advent of newer and better MEMS technology more improvements are expected than outlined in this work.

6.2 Recommendations

Based on the results obtained herein, the following recommendations for future investigations are made:

1) The system developed herein was tested for pedestrian applications. However, it can also be tested for use in vehicle applications. The angular accelerations obtained directly from a GFIMU are valuable for detection of impending rollover in crash situations (Schopp et al 2010). Furthermore, many safety and control applications in a vehicle utilize inertial sensors, for example, airbag control

systems, anti-theft systems, and vehicle navigations systems. These systems, however, mostly work independently. Therefore, by combining the accelerometer sensors from different units, GFIMU measurements could be combined, which might lead to cost reduction and increased reliability.

2) This work dealt with integration of GPS with Gyroscope-free inertial navigation for pedestrian applications. However, pedestrian dead reckoning (PDR) is often used for pedestrian applications. It would be interesting to see the performance achieved using GPS/PDR integration.

3) Better scale factor estimation in the GFIN+ EKF approach could lead to more improvements. In this work, a coarse estimate of scale factor of the MEMS accelerometers was obtained during the calibration. However, if the scale factor of the accelerometers and the gyroscope used were determined in the EKF, improvement should occur.

4) The biases in the EKF were modeled using a Gauss Markov process. Further investigations may involve the use of Autoregressive (AR) processes to model the residual biases. This might further improve the results.

5) The GPS/GFIN+ integrated system was used in post mission, which is ideal for testing and development. However, offline processing techniques like optimal smoothing, Kalman filter tuning are unavailable to real-time systems. Owing to the growing demands for real-time position and navigation information, a more thorough analysis of GPS/GFIN+ integrated system in the real-time environment is desirable.

6) Statistical reliability quantifies what magnitude of errors can be detected and removed by a system. An erroneous measurement can bias the estimated parameters, thus compromising system integrity. Therefore, investigating reliability in the integrated system is very important, as it has a direct impact on system performance.

7) Many other accelerometer configurations have been proposed by other researchers and could be tested. These vary on the basis of the number and placement of accelerometers in the configuration. Researchers like Schuler et al (1967) and Williams & Fyfe (2004) have discussed the requirements needed for a feasible configuration. The use of such configurations would allow testing the integration algorithm designed in this thesis.

8) In this work Crista MEMS gyroscope was used to combine with the accelerometer configuration. However, if a lower quality gyroscope is used, it would lead to more weight on the accelerometer angular estimates than gyroscope measurement. Therefore, accelerometer-derived angular estimates would be used in the final estimation of angular velocity. Thus, testing the algorithm with a lower quality gyroscope is recommended.

References

Ang W. T., P. K. Khosla, C. N. Riviere (2003) "Design of all-accelerometer inertial measurement unit for tremor sensing in hand-held microsurgical instrument", *in Proceedings of IEEE International Conference on Robotics and Automation*, pp. 1781-1786.

Bancroft, J., G. Lachapelle, M. E. Cannon, M. G. Petovello, "Twin IMU-HSGPS Integration for Pedestrian Navigation" in *Proceedings of ION GNSS 2008,* 16-20 Sept., Savannah, Georgia.

Bayard, D. and S. Ploen (2005) "High Accuracy Inertial Sensors from inexpensive components", US Patent.

Brown, R. and P. Hwang (1997) *Introduction to Random Signals and Applied Kalman Filtering*. Wiley.

Bruton, A. M., K. P. Schwarz, J. Skaloud (2000) "The use of wavelets for analysis and de-noising of kinematic geodetic measurements" *Proceedings of the IAG Symposia No. 121, Geodesy Beyond 2000: The Challenges of the First Decade*, Birmingham, UK.

Cardou, P. and J. Angeles (2008a) "Angular velocity estimation from the angular acceleration matrix" *Journal of Applied Mechanics*, vol. 75, no. 2, pp. 021003-1 – 021003-8.

Cardou, P. and J. Angeles (2008b) "Estimating the angular velocity of a rigid body moving in the plane from tangential and centripetal acceleration measurements" *Multibody System Dynamics*, Vol. 19, No. 4, pp. 383-406.

Chen, J.-H., S.-C. Lee and D. DeBra (1994) "Gyroscope free strapdown inertial measurement unit by six linear accelerometers" *Journal of Guidance, Control and Dynamics*, vol. 17, no. 2, pp. 286-290.

Costello, M., T. Jitpraphai (2002) "Determining Angular Velocity and Angular Acceleration of projectiles using triaxial acceleration measurements" *Journal of spacecraft and rockets*, Vol. 39, pp.73-80.

Crista-Interface/Operation Document (2009) *Crista Inertial Measurement Unit (IMU) Interface/Operation Document,* Cloud Cap Technology Inc.

Digi-Key (2010), http://search.digikey.com/scripts/DkSearch/dksus.dll last accessed July 27, 2010.

Dolabdjian, Ch., J. Fadili, and E. Huertas Levya (2002) "Classical Low Pass Filter and Real-Time Wavelet-Based Denoising technique implemented on a DSP: a comparison study", EPJ Applied Physics.

ElHabiby, M.M. (2007) *Wavelet Representation of Geodetic Operators*, PhD Thesis, Department of Geomatics Engineering, University of Calgary, Canada, UCGE Report No. 20250.

El-Sheimy, N. (2009) *Inertial techniques and INS/DGPS Integration*, ENGO 623- Course Notes, Department of Geomatics Engineering, University of Calgary, Canada.

FCC (2010) http://www.fcc.gov/pshs/services/911-services/enhanced911/Welcome.html last accessed on November 9, 2010.

Filho E. A. M., H. K. Kuga, A. R. Neto (2006) "Integrated GPS/INS Navigation System Based on a Gyroscope-Free IMU" Brazilian Conference on Dynamics, Control and Their Applications, May 22-26, Guaratimgueta, SP, Brazil.

Giansanti, D., V. Macellari, G. Maccioni and A. Cappozzo (2003) "Is it feasible to reconstruct body segment 3-D position and orientation using accelerometric data?" *IEEE Transactions on Biomedical Engineering*, vol. 50, no. 4, pp. 476-483.

Godha, S. (2006) *Performance Evaluation of Low Cost MEMS-Based IMU Integrated With GPS for Land Vehicle Navigation Application,* MSc Thesis, Department of Geomatics Engineering, University of Calgary, Canada, UCGE Report No. 20239.

Graps, A. (2004) *An Introduction to Wavelets*,

http://www.amara.com/IEEEwave/IEEEwavelet.html last accessed January 31, 2010.

Groves, P. D., G. W. Pulford, C. A. Littlefield, D. L. J. Nash, C. J. Mather (2007) "Inertial Navigation Versus Pedestrian Dead Reckoning: Optimizing the Integration", in Proceedings of ION GNSS 20th International Technical Meeting of the Satellite Division, 25-28 September, Fort Worth, TX.

Guo, H., M. Yu, J. Liu, and J. Ning (2004) "Butterworth Low-Pass Filter for Processing Inertial Navigation System Raw Data" *Journal of Surveying Engineering*, November 2004.

Hamid, W.A. (2005) *Accuracy Enhancement of Integrated MEMS-IMU/GPS Systems for Land Vehicular Navigation Applications*, PhD Thesis, Department of Geomatics Engineering, University of Calgary, Canada, UCGE Report No. 20207.

Hide, C. (2003) *Integration of GPS and Low Cost INS Measurements,* PhD Thesis, Institute of Engineering, Surveying, and Space Geodesy, The University of Nottingham, UK.

IEEE Spectrum (2010) *STMicroelectronics Makes 3-Axis Digital Gyroscope with One Sensor*, http://spectrum.ieee.org/consumer-electronics/gadgets/stmicroelectronics-makes-3axis-digital-gyroscope-with-one-sensor, last accessed August 30, 2010.

Jansen, M. (2000) *Wavelet Thresholding and Noise Reduction*, PhD Thesis, Department of Computer Science, Katholieke Universiteit Leuven, Heverlee, Belgium.

Kane, T. R., D. A. Levinson (1985) *Dynamics, Theory and Applications*, McGraw Hill.

Kappi, J., J. Syrjarrine, J. Saarinen (2001) MEMS-IMU Based Pedestrian Navigator for Handheld Devices, *Proceedings of ION GPS*, Salt Lake City, UT, pp. 1369-1373.

Kennedy, S. and J. Rossi (2008) 'Performance of a deeply coupled commercial grade GPS/INS system from KVH and NovAtel Inc.' in Position, Location and Navigation Symposium. IEEE/ION.

Krishnan, V. (1965) "Measurement of Angular Velocity and Linear Acceleration using Linear Accelerometers", *Journal of the Franklin Institute*, October, Vol. 280, No. 4, pp. 307-315.

Kwakkel, S. (2008) *Human Lower Limb Kinematics Using GPS/INS,* MSc Thesis, Department of Geomatics Engineering, University of Calgary, Canada, UCGE Report No. 20279.

Lachapelle, G. (2008) *Advanced GPS Theory and Applications*, ENGO 625 Course Notes, Department of Geomatics Engineering, University of Calgary, Canada.

Lachapelle G., S. Godha, and M.E. Cannon (2006) "Performance of Integrated HSGPS-IMU Technology for Pedestrian Navigation under Signal Masking" in *Proceedings of European Navigation Conference,* 8-10 May, Royal Institute of Navigation, Manchester, U.K.

Mallat, S., C. Mallat (1999) *Wavelet Tour of Signal Processing (2nd Edition)* – Academic Press.

Meyer, Y., D. H. Salinger (1995) *Wavelet and Operators, Volume 1* – Cambridge University Press.

Misra, P. and P. Enge (2004) *Global Positioning System – Signals, Measurements, and Performance* – Ganga - Jamuna Press.

Misiti, M.; Y. Misiti; G. Oppenheim and J.M. Poggi (2009) *Wavelet Toolbox for the use with MATLAB*, The MathWorks Inc., MA, USA.

Mital, N. and A. King (1979) "Computation of rigid-body rotation in three dimensional space from body-fixed linear acceleration measurements" *Journal of Applied Mechanics*, vol. 46, pp. 925-930.

Mostov, K. S., A. A. Soloviev, T.-K. John Koo (1998) "Accelerometer based Gyro-Free Multi-Sensor Generic Inertial Device for Automotive Applications" *Proceedings of IEEE Conference on Intelligent Transportation System*, pp. 1047-1052.

Nassar, S. (2003) *Improving the Inertial Navigation System (INS) Error Model for INS and INS/DGPS Applications*, PhD Thesis, Department of Geomatics Engineering, University of Calgary, Canada, UCGE Report No. 20183.

Padgaonkar, A.J., K. W. Krieger, A. I. King (1975) "Measurement of Angular Acceleration of a Rigid Body Using Linear Accelerometers", Journal of Applied Mechanics, Vol. 42, pp. 552-556.

Park, S., C-W Tan (2002) "GPS-Aided Gyroscope-Free Inertial Navigation Systems" California Path Research Report, Institute of Transportation Studies, University of California, Berkeley.

Park, S., C-W Tan, J. Park (2005) "A scheme for improving the performance of a gyroscope-free inertial measurement unit" *Sensor and Actuators*, A 121, pp. 410-420.

Parsa, K., J. Angeles and A. K. Misra (2004) "Rigid-body pose and twist estimation using an accelerometer array" *Archive of Applied Mechanics*, vol. 74, pp. 223-236.

Pedestrian crossing clip art, http://www.clker.com/clipart-map-symbols-pedestrian-crossing-black.html last accessed June 22, 2010.

Petovello, M. (2003) *Real-time Integration of a Tactical-Grade IMU and GPS for High-Accuracy Positioning and Navigation,* PhD Thesis, Department of Geomatics Engineering, University of Calgary, Canada, UCGE Report No. 20173.

Polikar, R. (1996) *The Wavelet Tutorial*. Rowan University, College of Engineering Web

Server, http://users.rowan.edu/~polikar/WAVELETS/WTtutorial.html, Glassboro, New Jersey, USA last accessed March 09, 2009.

Schopp, P., L. Klingbeil, C. Peters, Y. Manoli (2010) "Design, Geometry evaluation, and calibration of a gyroscope-free inertial measurement unit" *Sensors Actuators A: Phys.*

Schuler, A., A. Grammatikos and K. Fegley (1967) "Measuring rotational motion with linear accelerometers" *IEEE Transactions on Aerospace and Electronic Systems*, vol.3, no. 3, pp. 465-472.

Shin, E. (2001) *Accuracy Improvement of Low Cost INS/GPS for Land Application*, MSc Thesis, Department of Geomatics Engineering, University of Calgary, Canada, UCGE Report No. 20156.

Skaloud, J (1999) *Optimizing Georeferencing of Airborne Survey Systems by INS/DGPS*, PhD Thesis, Department of Geomatics Engineering, University of Calgary, Canada, UCGE Report No. 20126.

Strang G., and T. Nguyen. (1996) *Wavelets and Filter Banks*, Wellesley-Cambridge Press.

United States Naval Observatory (USNO) (2010)

ftp://tycho.usno.navy.mil/pub/gps/gpsb2.txt, last accessed on June 18, 2010.

Valens C., (2004) A Really Friendly Guide to Wavelets,

http://pagesperso-orange.fr/polyvalens/clemens/wavelets/wavelets.html, last accessed on March 09, 2009.

Van Diggelen, F. (1998) "GPS Accuracy: Lies, Damn Lies and Statistics" GPS World.

Weimann F., G. Abwerzger, and B. Hofmann-Wellenhof (2007), "A Pedestrian Navigation System for Urban and Indoor Environments," in Proceedings of ION GNSS, 25-28 Sep, Fort Worth TX.

Williams T., A. Pahadia, M. Petovello, and G. Lachapelle (2009), "Using Accelerometer Configuration to Improve the Performance of a MEMS IMU: Feasibility Study with a Pedestrian Navigation Application," in *Proceedings of ION GNSS 2009,* 22-25 Sept., Savannah, Georgia.

Zappa B., G. Legnani, A. van den Bogert, R. Adamini (2001), "On the Number and Placement of Accelerometers for Angular Velocity and Acceleration determination", *Transactions of the ASME*, September, Vol. 123, pp. 552-553.